DR. JAMES SIMMER (Orcid ID : 0000-0002-7192-6105)

Article type : Original Article

The Enamel Phenotype in Homozygous Fam83h Truncation Mice

Shih-Kai Wang[1a*], Yuanyuan Hu[1], Charles E. Smith[1,2], Jie Yang[1b], Chunhua Zeng[1c] Jung-Wook Kim[3], Jan C-C. Hu[1], and James P. Simmer[1*]

Author Affiliations:

[1]Department of Biologic and Materials Sciences, University of Michigan School of Dentistry, 1210 Eisenhower Pl., Ann Arbor, MI USA 48108.

[2]Department of Anatomy and Cell Biology, McGill University, 3640 University Street, Montreal, Quebec H3A 0C7, Canada.

[3]Department of Pediatric Dentistry & Dental Research Institute, School of Dentistry; Seoul National University, 101 Daehak-ro, Jongno-gu, Seoul, 03080, Korea.

Email addresses of authors:

shihkaiw@umich.edu; shihkaiw@ntu.edu.tw; yyhu@umich.edu; charles.smith@mcgill.ca; jackyang@umich.edu; denyj78@gmail.com; chunhuazeng@hotmail.com; pedoman@snu.ac.kr; janhu@umich.edu; jsimmer@umich.edu

Current Addresses:

[a]Department of Dentistry, National Taiwan University School of Dentistry, No.1, Changde St., Jhongjheng District, Taipei City 100, Taiwan R.O.C.

[b]Department of Pediatric Dentistry, School and Hospital of Stomatology, Peking University, 22 South Avenue Zhongguancun Haidian District Beijing 100081 P. R. China.

[c]Department of Genetics and Endocrinology, Guangzhou Women and Children's Medical Center, Guangzhou Medical University, Guangzhou, P.R. China 9 Jinsui Rd, Guangzhou, Guangdong, China 510623

Grant numbers

This study was supported by

NIDCR/NIH research grants DE019622 (JH) and DE027675 (JPS)

National Research Foundation of Korea (NRF) grant funded by the Korea government (NRF-2017R1A2A2A05069281) (J-WK)

NTUH (National Taiwan University Hospital) Grant 106-N3424 and MOST (Ministry of Science and Technology in Taiwan) Grant 107-2314-B-002-014 (S-KW).

***Corresponding authors:**

Shih-Kai Wang, DDS, PhD

Department of Dentistry, National Taiwan University School of Dentistry,

No.1, Changde St., Jhongjheng District, Taipei City 100, Taiwan R.O.C.

E-mail: shihkaiw@ntu.edu.tw

James P. Simmer DDS, PhD
Dept. of Biologic and Materials Sciences,
University of Michigan School of Dentistry,
1210 Eisenhower Pl, Ann Arbor, MI 48108
Email: jsimmer@umich.edu

Abstract

Background: Truncation FAM83H mutations cause human autosomal dominant hypocalcified amelogenesis imperfecta (ADHCAI), an inherited disorder characterized by severe hardness defects in dental enamel. No enamel defects were observed in Fam83h null mice suggesting Fam83h truncation mice would better replicate human mutations.

Methods: We generated and characterized a mouse model ($Fam83h^{Tr/Tr}$) expressing a truncated FAM83H protein (amino acids 1-296), which recapitulated the ADHCAI-causing human FAM83H p.Tyr297* mutation.

Results: Day14 and 7-week $Fam83h^{Tr/Tr}$ molars exhibited rough enamel surfaces and slender cusps resulting from hypoplastic enamel defects. The lateral third of the $Fam83h^{Tr/Tr}$ incisor enamel layer was thinner, with surface roughness and altered enamel rod orientation, suggesting disturbed enamel matrix secretion. Regular electron density in mandibular incisor enamel indicated normal enamel maturation. Only mildly increased post-eruption attrition of $Fam83h^{Tr/Tr}$ molar enamel was observed at 7-weeks. Histologically, the $Fam83h^{Tr/Tr}$ enamel organ, including ameloblasts, and enamel matrices at sequential stages of amelogenesis exhibited comparable morphology without overt abnormalities, except irregular and less evident ameloblast Tomes' processes in specific areas.

Conclusions: Considering $Fam83h^{-/-}$ mice showed no enamel phenotype, while $Fam83h^{Tr/Tr}$ (p.Tyr297*) mice displayed obvious enamel malformations, we conclude that FAM83H

truncation mutations causing ADHCAI in humans disturbs amelogenesis through a neomorphic mechanism, rather than haploinsufficiency.

KEYWORDS
Amelogenesis imperfecta, truncation mutation, neomorphic mechanism, knockout mouse, skin defects, hair defects

1 INTRODUCTION

FAM83H (family with sequence similarity 83 member H on chromosome 8q24.3; OMIM *611927) is a gene that was originally identified by gene prediction of human genome through computational biology (Marchler-Bauer et al., 2005). Based upon the predicted 1179 amino acids of human FAM83H protein, the only functional domain motif was the N-terminal domain (DUF1669) of unknown function that characterizes all eight members of the FAM83 protein family (Finn et al., 2016). Little attention was paid to the FAM83H gene until it was reported to cause autosomal dominant hypocalcified amelogenesis imperfecta (ADHCAI, OMIM #130900) (Kim et al., 2008). ADHCAI is a specific type of inherited dental enamel malformations in humans. The defective enamel is hypomineralized with a marked decrease in hardness and is lost following tooth eruption, which imposes esthetic and functional burdens on affected individuals (Wright, Deaton, Hall, & Yamauchi, 1995). However, in spite of the high prevalence of ADHCAI in North America and the many FAM83H mutations that have been identified in ADHCAI patients, the pathogenesis of this disease is largely unknown.

To date, 27 different FAM83H autosomal dominant truncation mutations have been associated with ADHCAI (Chan et al., 2011; Ding et al., 2009; El-Sayed, Shore, Parry, Inglehearn, & Mighell, 2010; Hart et al., 2009; Haubek et al., 2011; Hyun et al., 2009; Kantaputra, Intachai, & Auychai, 2016; Kim et al., 2008; Lee et al., 2008; Lee et al., 2011; Prasad et al., 2016; Song, Wang, Zhang, Yang, & Bian, 2012; Wang, Hu, Yang, Smith,

Richardson, et al., 2015; Wright et al., 2009; Wright et al., 2011; Xin, Wenjun, Man, & Yuming, 2017; Zhang, Song, & Bian, 2015). Seven of these mutations have been found in multiple families. A contribution to the genetic etiology of ADHCAI has also been proposed for two heterozygous missense mutations, p.Ser342Thr (Pourhashemi et al., 2014) and p.Gly557Cys (Urzua et al., 2015), but their role in ADHCAI causality should be considered with caution. According to the ExAC database, the p.Gly557Cys mutation has a minor allele frequency of 3.57% in the non-Finnish European population, suggesting that this mutation is most likely a neutral sequence variant, considering the rarity of ADHCAI. The p.Ser342Thr mutation has not been documented in the database, but the substituted amino acid is not highly conserved evolutionarily, and serine to threonine is usually not structurally significant and is predicted to be "benign" using the PolyPhen-2 prediction algorithm of functionality, suggesting that this mutation is also not likely to be disease-causing (Adzhubei, Jordan, & Sunyaev, 2013). Despite these 2 missense mutations, all the other disease-causing FAM83H mutations are either nonsense or frameshift mutations that generate a premature termination codon in the most 3-prime exon of FAM83H. The resulting FAM83H transcripts apparently do not undergo nonsense mediated decay and are translated into truncated FAM83H proteins that include only the N-terminal region of FAM83H and extending no less than 287 amino acids and no longer than 694 amino acids (out of 1179 amino acids in the full-length FAM83H protein). Neither truncation mutations outside of this specific region (287-694) nor other types of loss-of-function mutations seem to be disease-causing. For this evident mutational homogeneity, it has been suspected that a dominant negative effect or a gain of function, rather than haploinsufficiency, underlies the pathological mechanism of ADHCAI. We previously generated and characterized Fam83h null mice, further demonstrating this hypothesis (Wang, Hu, Yang, Smith, Richardson, et al., 2015). The lack of

evident enamel defects in Fam83h heterozygous or null mice suggested that FAM83H is not required for normal enamel development in mice. A simple decrease of FAM83H function, including haploinsufficiency and dominant negativity, is not the cause of defective enamel in human ADHCAI. Instead, the truncated FAM83H from the mutant allele appears to impair normal enamel development by executing certain "toxic" effects (neomorphism) in ameloblasts, which cause the observed dominant enamel malformations.

In order to discern the "toxic" effects of truncated FAM83H in ameloblasts and unravel the pathogenesis of human ADHCAI, we generated a mouse model ($Fam83h^{Tr/Tr}$) by knocking in a truncation mutant Fam83h allele expressing only the N-terminal 296 amino acids of the FAM83H protein to recapitulate the human FAM83H p.Tyr297* mutation in mice. By characterizing the enamel phenotypes of $Fam83h^{Tr/Tr}$ mice, we hypothesized potential disease mechanisms of ADHCAI at the cellular level and discussed difficulties and limitations of establishing a disease animal model to recapitulate a human disorder caused by neomorphic mutations.

2 MATERIALS AND METHODS

2.1 Generation of knockin mice ($Fam83h^{Tr}$)

The knockin construct was designed and the mice (species: Mus musculus, strain C57BL/6) were generated by Ozgene (Perth, Australia). The $Fam83h^{Tr}$ mouse was generated by replacing Exon 4 of the endogenous Fam83h gene with a mini-cDNA that introduced an early translation termination codon. The mini-cDNA was composed of the whole of Exon 4 of Fam83h and the first 154 bp of Exon 5 followed by multiple polyadenylation signals. The 154^{th} nucleotide of Exon 5 was mutated from a T to a G to introduce a stop codon (TAG) in the codon for Tyrosine

297 (TAT) of wild-type Fam83h. The targeted Fam83h allele ($Fam83h^{Tr}$) is transcribed using its native promoter and translated from its native initiation codon, but generates a transcript encoding an open reading frame containing only the first 296 codons of wild-type Fam83h, followed by multiple polyadenylation signals. This mutant transcript is predicted to produce a truncated mouse FAM83H protein (normally 1209 amino acids) with only the N-terminal 296 amino acids ($FAM83H^{1-296}$) within the natural physiological context of Fam83h expression in vivo. This mouse model mimics a specific human FAM83H disease-causing mutation, p.Tyr297*. The deleted Fam83h and inserted NLS-lacZ sequences are provided in Figs. S3-S4.

2.2 Physical assessment and photography

Heterozygous mutant ($Fam83h^{+/Tr}$) mice were mated to generate three mouse Fam83h genotypes (+/+, +/Tr, and Tr/Tr), which were then evaluated for their physical appearance, activity, growth rate, size difference, food intake, and fertility. The homozygous ($Fam83h^{Tr/Tr}$) mice were viable and fertile. For gross evaluation of the dental enamel, mice were put under anesthesia using isofluorane, and their incisors were inspected under a dissection microscope. 7-week-old mice were sacrificed and fixative-perfused with 4% paraformaldehyde (PFA). The mandibles were removed and sliced through the mental symphysis with a razor blade to generate hemimandibles. These were carefully dissected free of soft tissues under a stereoscopic microscope using tissue forceps and a spoon excavator. The hemimandibles were submerged in 1% NaClO for 5 min, rinsed, air dried, and photographed using a Nikon SMZ1000 dissection microscope equipped with a Nikon digital camera DXM1200 (Melville, NY).

2.3 Molar Histology

For histology of developing molars, Day 5, 11, and 14 mouse heads were quickly dissected free of skin, cut in half, and immersed in 4% PFA fixative overnight at 4 °C and decalcified at 4 °C by immersion in 1 L of 4.13% disodium EDTA (pH 7.3) with agitation. The EDTA solution was changed every other day for 19–21 days for D11 mice, and 30 days for D14 mice. The samples were washed in PBS at 4 °C 4–5 times (every 0.5–1 h) followed by one overnight wash. The samples were dehydrated using a graded ethanol series followed by xylene, embedded in paraffin, and sectioned at 5 μm thickness. For staining, the sections were rehydrated and stained with hematoxylin and eosin (H&E) stain.

2.4 Incisor Histology

Fam83h$^{+/+}$, Fam83h$^{+/Tr}$, and Fam83h$^{Tr/Tr}$ mice at 7 weeks were deeply anesthetized with isoflurane, fixed by cardiac perfusion with 2.5% glutaraldehyde in 0.1 M sodium cacodylate buffer (pH 7.2–7.4) containing 0.05% calcium chloride, postfixed for 2 h at 4 °C, and rinsed 3x for 15 min each with 0.1 M sodium cacodylate buffer. The samples were decalcified at 4°C by immersion in 4 L of 4.13% disodium ethylenediaminetetraacetic acid (EDTA, pH 7.3) with agitation. The EDTA solution was changed every other day for 30 days. The samples were washed in PBS at 4 °C 4–5 times every 0.5–1 h, washed overnight, postfixed for 2 h in 1% osmium tetroxide/1.5% potassium ferrocyanide, dehydrated using an acetone gradient, embedded in Epon812 substitute, semi thin-sectioned and stained with 0.1% toluidine blue as described elsewhere (Smith, Hu, et al., 2011). Three maxillary (one from each genotype), 2 Fam83h$^{+/+}$, 2 Fam83h$^{+/Tr}$, and 5 Fam83h$^{Tr/Tr}$ mandibular incisors were processed for longitudinal sectioning. Three Fam83h$^{+/+}$ and 4 Fam83h$^{Tr/Tr}$ mandibular incisors were processed for cross sectioning at 1 mm increments as described previously (Hu et al., 2016).

2.5 Sodium Dodecyl Sulfate Polyacrylamide Gel Electrophoresis (SDS-PAGE)

The detailed protocol of protein extraction from mouse molars and the analyses were previously described (Wang, Hu, Yang, Smith, Nunez, et al.; Yamakoshi et al., 2011). Briefly, Mouse maxillary and mandibular first Fam83h$^{+/+}$; Fam83h$^{+/Tr}$; Fam83h$^{Tr/Tr}$; Fam83h$^{-/Tr}$ molars were extracted from mouse pups at D5, D11, and D14 using a dissecting microscope, stripped of soft tissue, and the mineralized portion of the teeth was incubated in 1 mL of 0.17 N HCl/0.95% formic acid for 2 h at 4 °C. After the undissolved materials were removed, the crude protein extract was buffer exchanged with 0.01% formic acid. The concentrate containing proteins extracted separately from the 4 molar genotypes was raised back to 250 μL of 0.01% formic acid and used for subsequent analysis by SDS-PAGE stained with Coomassie Brilliant Blue (CBB). The amount of protein applied per lane for SDS-PAGE was ~1/6 of the extract from a single molar. Recombinant mouse amelogenin (rM179) was used as a size control (Simmer et al., 1994).

2.6 Backscattered scanning electron microscopy

The procedures of backscattered scanning electron microscopy (bSEM) were described previously (Smith, Richardson, et al., 2011). Soft tissue was removed from the left and right hemimandibles of 7-week-old mice, and cross-sectioned at 1 mm increments from the basal (growing) end of the incisors and imaged by bSEM using a JOEL 7800 SEM at 20 kV (JOEL USA, Inc; Peabody, MA, USA). For whole incisor surface imaging, the bony soft tissue and bony caps covering the mandibular incisors were carefully removed and examined at 50X magnification with a Hitachi S-3000N variable pressure SEM using the backscatter mode at 25 kV and 20 pascal pressure.

For molar surface SEM, the molars were prepared as follows: The D14 hemimandibles were submerged in 4% PFA overnight, carefully dissected of soft tissues under a stereoscopic microscope, submerged in 1% NaClO for 20 min, rinsed, and acetone dehydrated (30%, 50%, 70%, 80%, 90%, 100%). The hemimandibles were mounted on metallic stubs using conductive carbon cement and carbon coated to increase conductivity and examined using a Hitachi (Century City, Los Angeles, CA) S-3000N variable pressure SEM using the backscatter mode.

2.7 Hardness Evaluations

The procedures for tissue preparation and microhardness testing were previously described (Wang, Hu, Yang, Smith, Nunez, et al.). In brief, hemimandibles from 7-week-old mice were cleaned free of soft tissue and embedded in Epon resin following graded acetone dehydration. After polymerization at 60 °C, the incisors were cross-sectioned 8 mm from the apical end of the incisor, approximately at the level of the crest of the alveolar bone close before the incisor erupts into the mouth. The cross-sectioned incisor was re-embedded in Castolite AC (Eager Polymers, Chicago, IL) using 25-mm SteriForm molds (Struers Inc., Westlake, OH), allowed to harden overnight, and polished.

Microhardness testing was performed using a LM247AT microhardness tester (Leco Corp., St. Joseph, MI) with a load of 25 g for 10 sec with a Knoop tip to obtain a Knoop hardness number (KHN). Measurements were made at 500X magnification. Indentations were placed in the outer, middle, and inner enamel as well as the dentin as a control reading for a total of four indentations per row. This series was performed three times in each animal, for a total of twelve points per animal. Hardness Data points were treated as independent, unweighted numbers and subjected to one-way ANOVA than Tukey's HSD test using calculation spreadsheet at http://vassarstats.net/anova1u.html. Statistical significance was determined at $p<0.01$.

Nano hardness test was done on (Hysitron TI 950 Triboindenter, Hysitron-Bruker, Minneapolis, MN, USA). Using the nano DMA indenter, the loading force was 8000 µN, 15 indents on each incisor spread among dentin, inner enamel, middle enamel and outer enamel. The data was analyzed by using Hysitron Troboscan.

2. 8 Micro-computed tomography (µCT)

Sample preparation and imaging process for micro-computed tomography (µCT) were conducted as previously described (Yang et al., 2015). Briefly, the agarose-embedded hemimandibles were scanned at 8 µm and analyzed with the SCANCO µCT-100 series micro-computed tomography system. The data were analyzed using the MiiL program (Medical Image Illustrator; National Applied Research Laboratories, Taipei, Taiwan). For calculating the hard tissue volumes from the 3D molar images, the contour of each first molar was outlined by marking the border of the tooth on each scanning section. 3D images were generated within the contour defined area. Based upon the distinct radiodensity of each tissue, the enamel, dentin, and pulp of the molars were isolated using density threshold ranges to measure the tissue volumes. The threshold range for measuring the pulp was 0 to 136, for dentin was 137 to 225, and for enamel was 226 to 255. The volume of each tissue was calculated using the MiiL Program and the volume within the defined area of each tooth that corresponded to the threshold ranges described above. The total volume of the whole tooth was the sum of volumes from its enamel, dentin, and pulp. The proportion of each tissue within a tooth was then calculated. The volume ratios of enamel to dentin (E/D) and enamel to dentin-pulp complex (E/D+P) were also evaluated.

3 RESULTS

3.1 Generation of truncated Fam83h-knockin mice

In order to recapitulate human FAM83H disease-causing mutations and investigate the pathogenesis of human ADHCAI, we generated a mouse model expressing a truncated (Tr) FAM83H protein in the C57BL/6-background. The structures of the Fam83h wild-type gene, the Fam83h targeting construct, the Cre-inverted intermediate, and the final Fam83h^{Tr} gene and strategy for PCR genotyping are provided in Fig. S1. We also provide relevant DNA sequences, such as the wild-type mouse Fam83h gene sequence and structure (Fig. S2), the knockin intermediate following removal of the selection genes by Flp-FRT recombination (Fig. S3), and the final Fam83h^{Tr} knockin sequence (Fig. S4).

Intercrosses of heterozygous (Fam83h$^{+/Tr}$) mice produced pups of three genotypes at the expected Mendelian ratio. The homozygous (Fam83h$^{Tr/Tr}$) mice were viable and fertile. At birth, they were indistinguishable from their wild-type (Fam83h$^{+/+}$) and heterozygous (Fam83h$^{+/Tr}$) littermates. However, when inspected at 7-weeks, the homozygous mutants (Fam83h$^{Tr/Tr}$) appeared normal in size but exhibited a sparse and scruffy coat, which allowed them to be readily discerned from their heterozygous and wild-type littermates. Despite the coat distinctness of 7-week Fam83h$^{Tr/Tr}$ mice, their incisors, when inspected under a dissection microscope (Fig. 1), appeared normal with glossy enamel surfaces and sharp incisal tips, comparable to those of their Fam83h$^{+/Tr}$ and Fam83h$^{+/+}$ littermates. However, when carefully viewed from the lateral perspective (Fig. 1B), the incisor enamel did not show a normal color of glazy yellow and a continuous curved line of light reflection, but instead exhibited a dull-white appearance with disrupted patchy areas of light reflection. Basic tooth morphology looked comparable among the three genotypes, although the molar enamel surface textures were not as smooth as those of the wild-type mice (Fig. 1C). Notably the extensive post-eruption attrition of enamel that is pathognomonic of the ADHCAI phenotype caused by heterozygous FAM83H truncation

mutations in humans was absent from the mouse heterozygous molars and mild even in the Fam83h$^{Tr/Tr}$ molars.

3.2 Enamel defects in Fam83h$^{Tr/Tr}$ molars

To assess the potential enamel phenotypes in detail, we examined 7-week molars by backscattered scanning electron microscopy (bSEM) (Fig. 2; Fig. S5). The basic morphology of the molars was comparable in the three genotypes, although the Fam83h$^{Tr/Tr}$ molars sometimes appeared to be mildly smaller than the Fam83h$^{+/Tr}$ and Fam83h$^{+/+}$ molars, and their cusps seemed slender compared to those of the Fam83h$^{+/Tr}$ and Fam83h$^{+/+}$ mice, suggesting that their enamel layer might be thinner. The Fam83h$^{Tr/Tr}$ molar surfaces were less smooth than those of the Fam83h$^{+/Tr}$ and Fam83h$^{+/+}$ molars, confirming the impression made under dissection microscope. When inspected from the occlusal view, the cusp tips of Fam83h$^{Tr/Tr}$ first molars exhibited only slightly larger wear facets, suggesting that the Fam83h$^{Tr/Tr}$ molars had undergone similarly mild attrition relative to the Fam83h$^{+/Tr}$ and Fam83h$^{+/+}$ molars.

We removed the overlying soft tissue covering the unerupted (but nearly erupted) Day 14 molars and characterized them by bSEM (Fig. 3). The unerupted Fam83h$^{Tr/Tr}$ molars were similar to the 7-week Fam83h$^{Tr/Tr}$ molars that had functioned in occlusion for 5 weeks by also exhibiting enamel surface roughness and cusp slenderness, indicating that these phenotypes resulted from developmental defects rather than post-eruption changes.

To better assess the possibilities of smaller molar size and thinner enamel suggested by the dissection and bSEM microscopy, we performed µCT analyses to measure the volumes of enamel, dentin, and pulp in mandibular first molars at Day 14. Specific ranges of µCT threshold values were set to isolate each tissue (pulp, dentin and enamel): 0-136 for pulp, 137-225 for dentin, and 226-255 for enamel. The means of the measurements were calculated from 6 wild-

type, 5 heterozygous, and 6 homozygous D14 mice. There were no statistically significant differences in the volumes of the three dental tissues between the wild-type and heterozygous mice. In contrast, the total molar volume, and the volumes of dentin, enamel were reduced between the Fam83h$^{+/+}$ and the Fam83h$^{Tr/Tr}$ mice, and these differences were statistically significant (Fig. 4). The total tooth, dentin, and enamel volumes decreased to 84%, 87%, 62% of those of the wild-type, respectively. Overall, the mandibular first molars of the Fam83h$^{Tr/Tr}$ mice were smaller than those of the wild-type. As the proportion of dentin increased in the homozygous (77%) relative to the wild-type (75%), while the proportion of enamel fell in the homozygous (9.7%) relative to the wild-type (13.2%), it is evident that the Fam83h$^{Tr/Tr}$ molars are smaller than those of the wild-type principally because of a reduction in enamel volume, confirming a hypoplastic enamel defect in Fam83h$^{Tr/Tr}$ molars.

We analyzed the histology of developing maxillary first molars at postnatal D5, D11, and D14 for three genotypes (Fig. 5, Fig. S6). All D5 first molars showed typical tall-columnar secretory stage ameloblasts with accumulation of eosinophilic extracellular matrices in the enamel. Similarly, in D11 first molars of all genotypes, the maturation stage ameloblasts appeared comparable adjacent to an enamel space with some residual matrix. At D14, when the molar was about to erupt into oral cavity, all molars of the three genotypes exhibited a thin layer of reduced enamel epithelium outlining the enamel space containing little residual matrix. Odontoblasts, developing dentin-pulp complexes, developing roots, and surrounding periodontal tissues of D5, D11, and D14 first molars seemed to be comparatively normal in Fam83h$^{+/Tr}$, and Fam83h$^{Tr/Tr}$ mice. Light microscope histology of developing first molars did not provide evidence of pathology that could explain the enamel hypoplasia or surface roughness.

We also utilized SDS-PAGE to analyze crude protein extracts from D5, D11, and D14 first molars of Fam83h$^{+/+}$, Fam83h$^{+/Tr}$, and Fam83h$^{Tr/Tr}$ mice (Fig. S7). No clear differences in the amount of matrix proteins were observed among first molars of the different genotypes at D5, D11, and D14, which was consistent with the molar histology findings that ameloblast form and enamel architecture were not grossly altered in the Fam83h$^{+/Tr}$ and Fam83h$^{Tr/Tr}$ mice.

3.3 Enamel defects in Fam83h$^{Tr/Tr}$ mandibular incisors

The mineralization of mandibular incisors was analyzed by comparing backscattered scanning electron microscopy (bSEM) images of 1-mm incremental cross-sections (from level 2 to 8) progressing from early (apical) to late (incisal) stage of development along the continuously growing mandibular incisors from Fam83h$^{+/+}$, Fam83h$^{+/Tr}$, and Fam83h$^{Tr/Tr}$ mice. The incisor cross-sections from all levels were imaged at three magnifications and the three genotypes compared at each magnification. These magnifications (from low to high) show the entire incisor cross-sections (Fig. S8), the enamel layer and underlying dentin (Fig. S9), and the enamel layer at the height of contour (Fig. S10), where the enamel is thickest and its rod pattern most evident. These comparisons, along with the study of bSEM image panels showing six Fam83h$^{+/Tr}$ (Figs. S11-S16), six homozygous (Fam83h$^{Tr/Tr}$) (Figs. S17-S22), and one wild-type (Fam83h$^{+/+}$) (Fig. S23) incisors at 1 mm cross-sections at all three magnifications, demonstrated virtually normal progression of dentin and enamel mineralization in all three genotypes. The gist of these findings is evident in Fig. 6, which shows a panel of bSEM images of incisor cross-sections at level 8 that show the enamel layer after it had completed maturation and was about to erupt into the oral cavity. The enamel layer at level 8 in the WT, heterozygous (Fam83h$^{+/Tr}$) and homozygous (Fam83h$^{Tr/Tr}$) mice exhibited comparable thickness (from the DEJ to the enamel surface at the height of contour), electron density (reflecting degree of mineralization) and overall enamel rod

patterns at sequential sections among the three genotypes, indicating that expression of the truncated FAM83H protein did not interfere with enamel and dentin mineralization, making it unlikely that enamel matrix secretion was disturbed. However, when inspected carefully, the lateral (lateral) 1/3 of the enamel layer of Fam83h$^{Tr/Tr}$ incisors was thinner relative to the Fam83h$^{+/Tr}$ and Fam83h$^{+/+}$ incisors (Fig. 7). While the labial enamel surface of a normal incisor exhibited a smooth line gradually approaching the lateral cervical margin on a cross-section, the contour of Fam83h$^{Tr/Tr}$ enamel abruptly steepened down at the lateral 1/3. This was evident at incremental sections starting from level 4, which represented the post-secretory (maturation) stage of enamel formation. In contrast, the dentin and surrounding alveolar bone of mandibular incisors in all three genotypes appeared to be comparable on bSEM cross-sections.

To quantify this hypoplastic enamel defect, we analyzed the mesial and lateral enamel areas of level 8 cross-sections from ten Fam83h$^{+/+}$ and eight Fam83h$^{Tr/Tr}$ 7-week mandibular incisors (Fig. 8; Fig. S24). A bisecting line perpendicular to a line segment connecting the mesial cervical margin and the lateral cervical margin was used to divide the incisor enamel into mesial and lateral parts, and the areas of each part and the total enamel were calculated. In the wild-type incisor, the average area of total enamel was around 73,700 μm^2, roughly three-fifths (45,600 μm^2) of which was mesial enamel and two-fifths (28,100 μm^2) was lateral enamel. In contrast, the Fam83h$^{Tr/Tr}$ incisor exhibited significantly smaller areas of total and lateral enamel (66,800 μm^2 and 22,300 μm^2 respectively), but not mesial enamel (44,500 μm^2). While the mesial enamel area appeared to be comparable between the wild-type and Fam83h$^{Tr/Tr}$ incisors, the lateral enamel area of the Fam83h$^{Tr/Tr}$ incisor was less than 80% that of the wild-type incisor. This uneven reduction of enamel area changed the proportion of lateral to mesial enamel from

2:3 to 1:2, confirming a thickness defect in enamel on the lateral aspect of a Fam83h$^{Tr/Tr}$ mandibular incisor.

To assess potential alteration of enamel functionality in Fam83h$^{Tr/Tr}$ mice, we conducted Knoop hardness testing (KHT) and Nano hardness testing (NHT) of dentin, the inner enamel (near dentin), the middle enamel, and outer enamel (near the surface) on 7-week incisors of the three genotypes at level 8 (Fig. 9; Figs. S25-S27). However, neither Knoop hardness values nor Nano hardness values in respective areas of enamel among Fam83h$^{+/+}$, Fam83h$^{+/Tr}$, and Fam83h$^{Tr/Tr}$ mice showed a significant difference. All samples demonstrated a rising trend of hardness values from dentin to the enamel surface, with dentin being the lowest and outer enamel the highest. Noticeably, for NHT, we included two indentation locations (location N and location O; Fig. S26) at the lateral aspect of the incisor where we found reduced enamel thickness and altered rod-interrod structure. Nonetheless, the three genotypes exhibited comparable hardness values at both locations, indicating no apparent hardness defect at this area.

3.4 Histological analyses of Fam83h incisors at 7-weeks

We analyzed the histology of longitudinal sections of continuously growing maxillary (Figs. S28-S30) and mandibular (Figs. S31-S48) incisors of 7-week Fam83h$^{+/+}$, Fam83h$^{+/Tr}$, and Fam83h$^{Tr/Tr}$ mice, which exhibited all stages of enamel formation. The basic morphology of the enamel organ, including ameloblasts, and enamel matrices at differentiation, secretory, transition, and maturation stages appeared comparable in the three genotypes, although the secretory-stage ameloblasts of Fam83h$^{Tr/Tr}$ incisor gave the impression of being shorter, with a likely increased nucleus-to-cell height ratio, compared to those of Fam83h$^{+/+}$ and Fam83h$^{+/Tr}$ incisors (Fig. 10). The Fam83h$^{Tr/Tr}$ incisor also exhibited normal onset of ameloblast differentiation and transition through all stages of amelogenesis without apparent delay, advance,

or interruption. Furthermore, a clear enamel space with no residual staining was consistently observed beneath late maturation stage ameloblasts (Figs. S28, S32, S34, S36, S38 and S40), which indicated that the process of enamel maturation in the Fam83h$^{Tr/Tr}$ incisor had proceeded normally.

Being aware of a hypoplastic defect at the lateral aspect of Fam83h$^{Tr/Tr}$ incisor, we examined the histology of amelogenesis in 1-mm incremental cross-sections (from level 1 to 10; Figs. S49-S56) analogous to the previously-mentioned bSEM analyses, including high magnification montages of the incisor cross sections (Figs S57-S61). Ameloblasts reverse their secretory polarity during differentiation to allow for extracellular release of large amounts of proteins from plasma membrane surfaces that were originally the embryonic bases of the cells (Smith & Nanci, 1995). In general, level 1 showed the onset of secretory stage with elongated ameloblasts being reversely-polarized and developing Tomes' processes, while the mid-secretory stage could be observed at level 2 showing tall columnar ameloblasts with well-established Tomes' processes tilting mesially or laterally. The transition stage usually appeared around level 3, followed by the maturation stage extending from levels 3 through 8. With gradual removal of enamel matrix proteins and increased mineralization throughout the maturation stage, staining of the enamel matrix was barely observed after level 5. Consistent with the findings from longitudinal sections, the Fam83h$^{Tr/Tr}$ incisors exhibited comparable histology without overt morphological abnormalities at all section levels, relative to the Fam83h$^{+/+}$ incisors. However, at level 2 (mid-secretory stage), the ameloblasts over the lateral aspect of Fam83h$^{Tr/Tr}$ incisor showed less evident Tomes' processes than those of wild-type at the comparable area (Fig. 11). Also, in some Fam83h$^{Tr/Tr}$ samples, the Tomes' processes of ameloblasts at the central area of level 2 were irregular in the enamel layer, which was rarely observed in the wild-type samples

(Compare the wild-type Level 2 ameloblasts near the lateral cervical margin of Fig. S57 to the Fam83h$^{Tr/Tr}$ ameloblasts in the same position in Figs. S58-S61).

4 DISCUSSION

We recently demonstrated that Fam83h null mice exhibited no overt enamel defects, which suggested a non-essential role for FAM83H in enamel formation and supported a neomorphic disease mechanism of human autosomal dominant hypocalcified amelogenesis imperfecta (ADHCAI) (Wang, Hu, Yang, Smith, Richardson, et al., 2015). An amorphic (loss of function) disease mechanism for ADHCAI is ruled out in humans because only truncation mutations in a specific region of the last exon cause ADHCAI, whereas missense mutations in conserved positions and nonsense mutations in other parts of the gene that could cause a loss of function are not observed in ADHCAI patients. In mice, an amorphic mechanism for ADHCAI is ruled out because the Fam83h heterozygous and null mice do not exhibit an enamel phenotype (Wang, Hu, Yang, Smith, Richardson, et al., 2015). In this study we generated knockin (Fam83h$^{Tr/Tr}$) mice with a truncation defect (p.Tyr297*) homologous to those that cause human ADHCAI. The (Fam83h$^{Tr/Tr}$) mouse molars showed rough enamel surfaces and slender cusps while mandibular incisors showed enamel hypoplasia in their lateral enamel, indicating disturbed matrix secretion during enamel formation.

The mainly hypoplastic phenotype of Fam83h$^{Tr/Tr}$ enamel indicated that the secretory stage was more affected by the truncated FAM83H protein than was the maturation stage. We previously showed that in mouse molars, Fam83h expression in ameloblasts was generally weak and barely detectable until the transition to the maturation stage (Wang, Hu, Yang, Smith, Richardson, et al., 2015). This inconsistency suggests that mouse secretory stage ameloblasts are

more highly vulnerable to the "toxic" effect of truncated FAM83H, given that their expression of the protein is low. Maturation stage ameloblasts were more resistant, since the molar enamel hardness of Fam83h$^{Tr/Tr}$ mice was only slightly reduced. Although Fam83h$^{Tr/Tr}$ enamel was malformed, the defects were considerably different from those observed in ADHCAI patients. In human ADHCAI, the enamel of affected individuals is of normal thickness in unerupted or newly erupted teeth, but is hypomineralized, soft, and undergoes rapid attrition following eruption. It is unknown if human ameloblasts express FAM83H at higher levels than mouse ameloblasts, which might account for the more severe enamel defects in ADHCAI patients. Alternatively, human ameloblasts, particularly the maturation stage ones, might be more sensitive to the "toxic" effect of the mutant FAM83H. This potential difference in FAM83H expression level and ameloblast susceptibility to the mutant protein might explain why enamel defects could be seen in homozygous (Fam83h$^{Tr/Tr}$), but not heterozygous (Fam83h$^{+/Tr}$) mutant mice, while a single copy of mutant FAM83H can cause ADHCAI in humans.

An interesting feature of Fam83h$^{Tr/Tr}$ incisors was that enamel defects were only evident on the lateral aspect. The mutant FAM83H protein in mice more significantly impacts appositional growth of enamel over the lateral aspect (of the incisor) than the mesial, causing a localized hypoplastic defect. In that area the enamel was thinner, but also the normal pattern of enamel rod rows was lost (Fig. 7). Interestingly, the altered Fam83h$^{Tr/Tr}$ incisor did not seem to affect enamel functionality, namely hardness, since we did not detect significant differences with either KHT or NHT.

Tomes' processes are cell projections of secretory stage ameloblasts into the enamel matrix. They are considered to be critical for establishment of enamel rod-interrod structure. Aberration of Tomes' processes on the lateral aspect of incisors might explain the hypoplastic

enamel in this area of Fam83h$^{Tr/Tr}$ incisors. Kuga et al. recently showed that FAM83H and its associated protein CK-1ε co-localized with keratin filaments in mouse ameloblasts, and demonstrated that FAM83H and CK-1 regulate the organization of the keratin cytoskeleton, and maintain the formation of desmosomes in human ameloblastoma cell lines (Kuga et al., 2016). Formation of Tomes' processes by ameloblasts reflects a significant reorganization of the cytoskeleton, so perhaps truncated FAM83H disturbs the organization of the cytoskeleton, although the normal FAM83H protein is not critical for proper organization of the keratin cytoskeleton in ameloblasts, given the fact that there are no evident enamel defects in Fam83h null mice (Wang, Hu, Yang, Smith, Richardson, et al., 2015).

Another interesting finding of Fam83h$^{Tr/Tr}$ enamel defects was that the molars appeared more affected and showed more prominent hypoplastic defects than the incisors did. This discrepancy might result from a fundamental difference in enamel structure between molars and incisors. The spatial distribution and three-dimensional arrangement of enamel types, namely schmelzmuster, in rodents have been well characterized and documented by paleontologists for phylogenetic purposes (von Koenigswald, 2004a, 2004b; von Koenigswald & Clemens, 1992). In most myomorph rodents, including mice (Mus musculus), the enamel microstructure of incisors comprises an inner layer of uniserial lamellar enamel (inner enamel) and an outer layer of radial enamel (outer enamel), as described above (Moinichen, Lyngstadaas, & Risnes, 1996; von Koenigswald & Clemens, 1992). The inner layer exhibits a decussation structure on cross sections and an architecture of Hunter-Schreger Bands (HSB) on sagittal (longitudinal) sections. On the other hand, the molars showed a more complicated enamel microstructure, named C-type schmelzmuster (von Koenigswald, 2004b). A basal ring of lamellar enamel (BRLE) surrounds the cervical part of the crown, covered by an outer layer of radial enamel, while the upper part of

the enamel cap is formed by mostly radial enamel with rods perpendicular to the enamel surface. The uniserial HSBs in incisors are identical to the BRLE in molars. The truncated FAM83H protein disturbed the ameloblast Tomes' processes and altered the enamel rod profiles they produced. The effects was more significant on radial enamel with rods perpendicular to the enamel surface, which comprise the greater part of a molar crown, contributing to the surface roughness of Fam83h$^{Tr/Tr}$ molars. In contrast, the incisor outer enamel with rods running parallel to the enamel surface might be less susceptible to the altered rod-interrod profile caused by truncated FAM83H and therefore exhibit a minor hypoplastic defect. Interestingly, mice with ablation of serotonin 2B receptor (Htr2b null mice) have a similar molar phenotype of generally thinner enamel with surface roughness, and the enamel microstructure and rod profiles of Htr2b$^{-/-}$ molars were also abnormal (Dimitrova-Nakov et al., 2014; Harichane et al., 2011). Although the alteration of the rod profiles of molar enamel was not well detailed, primarily due to the high complexity of molar enamel microstructure and a lack of standardized methodology for molar characterization, it was clearly indicated that enamel analysis of mutant genotypes based exclusively on incisor defects can be biased (Goldberg, Kellermann, Dimitrova-Nakov, Harichane, & Baudry, 2014). Correspondingly, the Fam83h$^{Tr/Tr}$ mice in this study also demonstrated distinct enamel phenotypes between incisors and molars, indicating a necessity of comprehensive characterization of both tooth types in a given mouse model and an imperativeness of developing standardized methods to investigate molar enamel microstructure.

We previous showed that Fam83h null mice died at around 2 weeks, and the few older survivors were generally weak, suggesting an essential role of FAM83H in certain critical physiological functions (Wang, Hu, Yang, Smith, Richardson, et al., 2015). Nonetheless, in this study, Fam83h$^{Tr/Tr}$ mice appeared to be viable and fertile. This discrepancy in viability suggested

that the N-terminal 296 amino acids of FAM83H is sufficient for its critical functions. In other words, the truncated part of the protein in the C-terminus, composed of about 900 amino acids, is not necessary for viability functions. The protein family of FAM83 is characterized by a highly conserved N-terminal domain of unknown function, DUF1669, comprising ~300 amino acids (Cipriano et al., 2014). Except for this domain, the 8 members of FAM83 family have vastly different C-terminal regions with variable lengths. The FAM83 proteins were recently identified as novel transforming oncogenes that function as intermediaries in EGFR/RAS signaling, and the oncogenic properties were dependent upon the conserved DUF1669 domain (Cipriano et al., 2012; Cipriano et al., 2014). It was also demonstrated that these proteins, including FAM83H, were overexpressed in many human tumors (Cipriano et al., 2014; Snijders et al., 2017). Therefore, FAM83H might play a role in cell proliferation or survival mediated by EGFR/RAS signaling, presumably through its DUF1669 domain, which is essential to certain critical physiological functions. In this regard, complete loss of FAM83H in Fam83h null mice would be fatal. In contrast, the Fam83h$^{Tr/Tr}$ mice, although only expressing the first 296 amino acids of FAM83H containing the DUF1669 domain, would be able to survive. In other words, for certain cells other than ameloblasts, the mutant (truncated) FAM83H protein is not only not "toxic", but can serve critical functions. Nevertheless, despite the viability, Fam83h$^{Tr/Tr}$ mice exhibited sparse and scruffy coat as did Fam83h null mice (Wang, Hu, Yang, Smith, Richardson, et al., 2015), which suggested that the DUF1669 domain of FAM83H was not sufficient to serve its functions in hair follicle cells. Since FAM83H is believed to interact with keratin through its C-terminus (Kuga et al., 2013), FAM83H might be critical for maintaining the homeostasis of hair follicles via this interaction. Therefore, loss of FAM83H C-terminus, in both Fam83h null and Fam83h$^{Tr/Tr}$ mice, leads to hair pathology.

ACKNOWLEGEMENTS

This work was supported by NTUH (National Taiwan University Hospital) Grant 106-N3424, MOST (Ministry of Science and Technology in Taiwan) Grant 107-2314-B-002-014, NIDCR/NIH grant 1R01DE015846 and 1R01DE27675.

CONFLICTS OF INTEREST

The authors have no conflicts of interest to declare regarding this manuscript.

REFERENCES

Adzhubei, I., Jordan, D. M., & Sunyaev, S. R. (2013). Predicting functional effect of human missense mutations using PolyPhen-2. Current Protocols in Human Genetics, Chapter 7, Unit7 20. https://doi.org/10.1002/0471142905.hg0720s76

Chan, H. C., Estrella, N. M., Milkovich, R. N., Kim, J. W., Simmer, J. P., & Hu, J. C. (2011). Target gene analyses of 39 amelogenesis imperfecta kindreds. European Journal of Oral Sciences, 119 Suppl 1, 311-323. https://doi.org/10.1111/j.1600-0722.2011.00857.x

Cipriano, R., Graham, J., Miskimen, K. L., Bryson, B. L., Bruntz, R. C., Scott, S. A., . . . Jackson, M. W. (2012). FAM83B mediates EGFR- and RAS-driven oncogenic transformation. Journal of Clinical Investigation, 122(9), 3197-3210. https://doi.org/10.1172/JCI60517

Cipriano, R., Miskimen, K. L., Bryson, B. L., Foy, C. R., Bartel, C. A., & Jackson, M. W. (2014). Conserved oncogenic behavior of the FAM83 family regulates MAPK signaling in human cancer. Molecular Cancer Research, 12(8), 1156-1165. https://doi.org/10.1158/1541-7786.MCR-13-0289

Dimitrova-Nakov, S., Baudry, A., Harichane, Y., Collet, C., Marchadier, A., Kellermann, O., & Goldberg, M. (2014). Deletion of serotonin 2B receptor provokes structural alterations of mouse dental tissues. Calcified Tissue International, 94(3), 293-300. https://doi.org/10.1007/s00223-013-9810-y

Ding, Y., Estrella, M. R., Hu, Y. Y., Chan, H. L., Zhang, H. D., Kim, J. W., . . . Hu, J. C. (2009). Fam83h is associated with intracellular vesicles and ADHCAI. Journal of Dental Research, 88(11), 991-996. https://doi.org/10.1177/0022034509349454

El-Sayed, W., Shore, R. C., Parry, D. A., Inglehearn, C. F., & Mighell, A. J. (2010). Ultrastructural analyses of deciduous teeth affected by hypocalcified amelogenesis imperfecta from a family with a novel Y458X FAM83H nonsense mutation. Cells Tissues Organs, 191(3), 235-239. https://doi.org/10.1159/000252801

Finn, R. D., Coggill, P., Eberhardt, R. Y., Eddy, S. R., Mistry, J., Mitchell, A. L., . . . Bateman, A. (2016). The Pfam protein families database: towards a more sustainable future. Nucleic Acids Research., 44(D1), D279-285. https://doi.org/10.1093/nar/gkv1344

Goldberg, M., Kellermann, O., Dimitrova-Nakov, S., Harichane, Y., & Baudry, A. (2014). Comparative studies between mice molars and incisors are required to draw an overview of enamel structural complexity. Frontiers in Physiology, 5, Article 359. https://doi.org/10.3389/fphys.2014.00359

Harichane, Y., Dimitrova-Nakov, S., Marchadier, A., Collet, C., Baudry, A., Vidal, C., . . . Goldberg, M. (2011). Enamel alterations in serotonin 2B receptor knockout mice. European Journal of Oral Sciences, 119(Suppl 1), 177-184. https://doi.org/10.1111/j.1600-0722.2011.00908.x

Hart, P. S., Becerik, S., Cogulu, D., Emingil, G., Ozdemir-Ozenen, D., Han, S. T., . . . Hart, T. C. (2009). Novel FAM83H mutations in Turkish families with autosomal dominant hypocalcified amelogenesis imperfecta. Clinical Genetics, 75(4), 401-404. https://doi.org/10.1111/j.1399-0004.2008.01112.x

Haubek, D., Gjorup, H., Jensen, L. G., Juncker, I., Nyegaard, M., Borglum, A. D., . . . Hertz, J. M. (2011). Limited phenotypic variation of hypocalcified amelogenesis imperfecta in a Danish five-generation family with a novel FAM83H nonsense mutation. International Journal of Paediatric Dentistry, 21(6), 407-412. https://doi.org/10.1111/j.1365-263X.2011.01142.x

Hu, Y., Smith, C. E., Richardson, A. S., Bartlett, J. D., Hu, J. C., & Simmer, J. P. (2016). MMP20, KLK4, and MMP20/KLK4 double null mice define roles for matrix proteases during dental enamel formation. Molecular Genetics & Genomic Medicine, 4(2), 178-196. https://doi.org/10.1002/mgg3.194

Hyun, H. K., Lee, S. K., Lee, K. E., Kang, H. Y., Kim, E. J., Choung, P. H., & Kim, J. W. (2009). Identification of a novel FAM83H mutation and microhardness of an affected molar in autosomal dominant hypocalcified amelogenesis imperfecta. International Endodontic Journal, 42(11), 1039-1043. https://doi.org/10.1111/j.1365-2591.2009.01617.x

Kantaputra, P. N., Intachai, W., & Auychai, P. (2016). All enamel is not created equal:Supports from a novel FAM83H mutation. American Journal of Medical Genetics Part A, 170A(1), 273-276. https://doi.org/10.1002/ajmg.a.37406

Kim, J. W., Lee, S. K., Lee, Z. H., Park, J. C., Lee, K. E., Lee, M. H., . . . Simmer, J. P. (2008). FAM83H mutations in families with autosomal-dominant hypocalcified amelogenesis imperfecta. The American Journal of Human Genetics, 82(2), 489-494. https://doi.org/10.1016/j.ajhg.2007.09.020

Kuga, T., Kume, H., Adachi, J., Kawasaki, N., Shimizu, M., Hoshino, I., . . . Tomonaga, T. (2016). Casein kinase 1 is recruited to nuclear speckles by FAM83H and SON. Scientific Reports, 6, 34472. https://doi.org/10.1038/srep34472

Kuga, T., Kume, H., Kawasaki, N., Sato, M., Adachi, J., Shiromizu, T., . . . Tomonaga, T. (2013). A novel mechanism of keratin cytoskeleton organization through casein kinase Ialpha and

FAM83H in colorectal cancer. Journal of Cell Science, 126(Pt 20), 4721-4731. https://doi.org/10.1242/jcs.129684

Lee, S. K., Hu, J. C., Bartlett, J. D., Lee, K. E., Lin, B. P., Simmer, J. P., & Kim, J. W. (2008). Mutational spectrum of FAM83H: the C-terminal portion is required for tooth enamel calcification. Human Mutation, 29, E95-E99. https://doi.org/10.1002/humu.20789

Lee, S. K., Lee, K. E., Jeong, T. S., Hwang, Y. H., Kim, S., Hu, J. C., . . . Kim, J. W. (2011). FAM83H mutations cause ADHCAI and alter intracellular protein localization. Journal of Dental Research, 90(3), 377-381. https://doi.org/10.1177/0022034510389177

Marchler-Bauer, A., Anderson, J. B., Cherukuri, P. F., DeWeese-Scott, C., Geer, L. Y., Gwadz, M., . . . Bryant, S. H. (2005). CDD: a Conserved Domain Database for protein classification. Nucleic Acids Research., 33(Database issue), D192-196. https://doi.org/10.1093/nar/gki069

Moinichen, C. B., Lyngstadaas, S. P., & Risnes, S. (1996). Morphological characteristics of mouse incisor enamel. Journal of Anatomy, 189(Pt 2), 325-333.

Pourhashemi, S. J., Ghandehari Motlagh, M., Meighani, G., Ebrahimi Takaloo, A., Mansouri, M., Mohandes, F., . . . Heidari, M. (2014). Missense Mutation in Fam83H Gene in Iranian Patients with Amelogenesis Imperfecta. Iranian Journal of Public Health, 43(12), 1680-1687.

Prasad, M. K., Geoffroy, V., Vicaire, S., Jost, B., Dumas, M., Le Gras, S., . . . Bloch-Zupan, A. (2016). A targeted next-generation sequencing assay for the molecular diagnosis of genetic disorders with orodental involvement. Journal of Medical Genetics, 53(2), 98-110. https://doi.org/10.1136/jmedgenet-2015-103302

Simmer, J. P., Lau, E. C., Hu, C. C., Aoba, T., Lacey, M., Nelson, D., . . . Fincham, A. G. (1994). Isolation and characterization of a mouse amelogenin expressed in Escherichia coli. Calcified Tissue International, 54(4), 312-319.

Smith, C. E., Hu, Y., Richardson, A. S., Bartlett, J. D., Hu, J. C., & Simmer, J. P. (2011). Relationships between protein and mineral during enamel development in normal and genetically altered mice. European Journal of Oral Sciences, 119 Suppl 1, 125-135. https://doi.org/10.1111/j.1600-0722.2011.00871.x

Smith, C. E., & Nanci, A. (1995). Overview of morphological changes in enamel organ cells associated with major events in amelogenesis. The International Journal of Developmental Biology, 39(1), 153-161.

Smith, C. E., Richardson, A. S., Hu, Y., Bartlett, J. D., Hu, J. C., & Simmer, J. P. (2011). Effect of kallikrein 4 loss on enamel mineralization: comparison with mice lacking matrix metalloproteinase 20. The Journal of Biological Chemistry, 286(20), 18149-18160. https://doi.org/10.1074/jbc.M110.194258

Snijders, A. M., Lee, S. Y., Hang, B., Hao, W., Bissell, M. J., & Mao, J. H. (2017). FAM83 family oncogenes are broadly involved in human cancers: an integrative multi-omics approach. Molecular Oncology, 11(2), 167-179. https://doi.org/10.1002/1878-0261.12016

Song, Y. L., Wang, C. N., Zhang, C. Z., Yang, K., & Bian, Z. (2012). Molecular characterization of amelogenesis imperfecta in Chinese patients. Cells Tissues Organs, 196(3), 271-279. https://doi.org/10.1159/000334210

Urzua, B., Martinez, C., Ortega-Pinto, A., Adorno, D., Morales-Bozo, I., Riadi, G., . . . Reyes, M. (2015). Novel missense mutation of the FAM83H gene causes retention of amelogenin and a mild clinical phenotype of hypocalcified enamel. Archives of Oral Biology, 60(9), 1356-1367. https://doi.org/10.1016/j.archoralbio.2015.06.016

von Koenigswald, W. (2004a). Enamel Microstructure of Rodent Molars, Classification, and Parallelisms, with a Note on the Systematic Affiliation of the Enigmatic Eocene Rodent Protoptychus. Journal of Mammalian Evolution, 11(2), 127-142. https://doi.org/10.1023/B:JOMM.0000041192.79808.52

von Koenigswald, W. (2004b). The three basic types of schmelzmuster in fossil and extant rodent molars and their distribution among rodent clades. Palaeontographica, Abteilung A, 270, 95-132.

von Koenigswald, W., & Clemens, W. A. (1992). Levels of complexity in the microstructure of mammalian enamel and their application in studies of systematics. [Review]. Scanning Microscopy, 6(1), 195-217.

Wang, S.-K., Hu, Y., Yang, J., Smith, C. E., Nunez, S. M., Richardson, A. S., . . . Simmer, J. P. (2015). Critical roles for WDR72 in calcium transport and matrix protein removal during enamel maturation. Molecular Genetics & Genomic Medicine, 3(4), 302-319. https://doi.org/10.1002/mgg3.143

Wang, S.-K., Hu, Y., Yang, J., Smith, C. E., Richardson, A. S., Yamakoshi, Y., . . . Simmer, J. P. (2015). Fam83h null mice support a neomorphic mechanism for human ADHCAI. Molecular Genetics & Genomic Medicine, 4(1), 46-67. https://doi.org/10.1002/mgg3.178

Warshawsky, H. (1971). A light and electron microscopic study of the nearly mature enamel of rat incisors. The Anatomical Record, 169(3), 559-583. https://doi.org/10.1002/ar.1091690307

Warshawsky, H., & Smith, C. E. (1971). A three-dimensional reconstruction of the rods in rat maxillary incisor enamel. The Anatomical Record, 169(3), 585-591. https://doi.org/10.1002/ar.1091690308

Wright, J. T., Deaton, T. G., Hall, K. I., & Yamauchi, M. (1995). The mineral and protein content of enamel in amelogenesis imperfecta. Connective Tissue Research, 32(1-4), 247-252.

Wright, J. T., Frazier-Bowers, S., Simmons, D., Alexander, K., Crawford, P., Han, S. T., . . . Hart, T. C. (2009). Phenotypic variation in FAM83H-associated amelogenesis imperfecta. Journal of Dental Research, 88(4), 356-360. https://doi.org/10.1177/0022034509333822

Wright, J. T., Torain, M., Long, K., Seow, K., Crawford, P., Aldred, M. J., . . . Hart, T. C. (2011). Amelogenesis imperfecta: genotype-phenotype studies in 71 families. Cells Tissues Organs, 194(2-4), 279-283. https://doi.org/10.1159/000324339

Xin, W., Wenjun, W., Man, Q., & Yuming, Z. (2017). Novel FAM83H mutations in patients with amelogenesis imperfecta. Scientific Reports, 7(1), 6075. https://doi.org/10.1038/s41598-017-05208-0

Yamakoshi, Y., Richardson, A. S., Nunez, S. M., Yamakoshi, F., Milkovich, R. N., Hu, J. C., . . . Simmer, J. P. (2011). Enamel proteins and proteases in Mmp20 and Klk4 null and double-null mice. European Journal of Oral Sciences, 119 Suppl 1, 206-216. https://doi.org/10.1111/j.1600-0722.2011.00866.x

Yang, J., Wang, S. K., Choi, M., Reid, B. M., Hu, Y., Lee, Y. L., . . . Hu, J. C. (2015). Taurodontism, variations in tooth number, and misshapened crowns in Wnt10a null mice and human kindreds. Mol Genet Genomic Med, 3(1), 40-58. https://doi.org/10.1002/mgg3.111

Zhang, C., Song, Y., & Bian, Z. (2015). Ultrastructural analysis of the teeth affected by amelogenesis imperfecta. Oral Surgery, Oral Medicine, Oral Pathology, Oral Radiology, and Endodontology, 119(2), e69-76. https://doi.org/10.1016/j.oooo.2014.09.002

FIGURE LEGENDS

Fig. 1. Photographs of Mouse Dentitions at 7-weeks. A: Frontal views of incisors. The teeth from all 3 genotypes look similar, with no signs of enamel chipping. **B:** Going clockwise from upper left for each genotype: lateral, mesial, lingual, labial views of a mandibular incisor. Arrowheads indicate the lateral surface of the incisor enamel where the Fam83h$^{Tr/Tr}$ mice show a dull white surface rather than the reflective yellow surface of the Fam83h$^{+/+}$ and Fam83h$^{+/Tr}$ mice. **C:** Occlusal, lingual, and buccal views of the mandibular incisors. All molars show normal crown morphology without evidence of attrition, although the Fam83h$^{Tr/Tr}$ molars exhibited a subtle roughness that reduced its luster.

Fig. 2. bSEM of Mandibular Molars at 7-weeks. The homozygous Fam83h$^{Tr/Tr}$ mice show a mildly rougher surface texture than the Fam83h$^{+/+}$ and Fam83h$^{+/Tr}$ mice. The first molars erupt into function after 2 weeks. By 7-weeks (shown here) signs of abnormal attrition are suggested by shorter, broader cusps. The Fam83h$^{Tr/Tr}$ first molar (on the right) shows mildly reduced cusp height in the lateral view and broadened cusp width in the occlusal view, suggesting mildly

increased attrition relative to the Fam83h$^{+/+}$ and Fam83h$^{+/Tr}$ mice. Similar bSEM views of other 7-week mouse molars from these genotypes are provided in Fig. S5.

Fig. 3. bSEM of D14 Mandibular Molars. Day 14 is the day before the first molar erupts into oral cavity and is often the last day that the developmental form of the molars can be observed prior to potential attrition from function. Lingual views are shown on the upper two panels, and occlusal views on the lower two panels. The crowns from all three genotypes are similar, but the homozygous Fam83h$^{Tr/Tr}$ molars display a rougher surface texture. Note in the occlusal views that the molar cusp tips are thin and pointed on all teeth, as they have not yet undergone occlusal wear.

Fig. 4. MicroCT Analyses of D14 Mandibular Molars. Day 14 precedes slightly the eruption of the first molar into function, before the potential effects of attrition on the volumes of enamel and dentin can occur. No statistically significant molar volumes were observed between the Fam83h$^{+/+}$ and Fam83h$^{+/Tr}$ and are not displayed. Total molar volume was reduced in the Fam83h$^{Tr/Tr}$ to 84% that of the wild-type. The volume of dentin was reduced by a lesser amount (to 87%), indicating that part of the total volume reduction was due to an overall reduction in tooth size. The volume of enamel was reduced in the Fam83h$^{Tr/Tr}$ to 62% that of the wild-type indicating that most of the reduction in molar size was due to a reduction in enamel volume.

Fig. 5. Histology of Fam83h$^{+/+}$ (WT), Fam83h$^{Tr/+}$, and Fam83h$^{Tr/Tr}$ Molars at Days 5, 11, and 14. **Key:** d, dentin; em, enamel matrix; *, ameloblasts.

Fig. 6. bSEM of 7-week Mandibular Incisor Cross Sections. These incisor cross sections show the enamel layer at a level near the crest of the alveolar bone (level 8), which is prior to eruption

into the oral cavity but after enamel has undergone extensive maturation. The enamel looks similar in the WT (+/+), heterozygous (+/Tr) and homozygous (Tr/Tr) mice. The enamel of the Fam83h$^{Tr/Tr}$ incisors appear to have normal centro-labial thickness, rod patterns and degree of mineralization. The only difference is in the contour of the enamel as it approaches the lateral side, so that the enamel layer is thinner than normal as it approaches the lateral cervical margin.

Fig. 7. bSEM of 7-week Mandibular Incisor Cross Sections. These incisor images are mosaics of cross sections imaged at high resolution. Note how the enamel layer thins prematurely as it approaches the lateral cervical margin and many of the enamel rods appear to be in the plane of section.

Fig. 8. Enamel area on 7-week mandibular incisor level 8 (alveolar crest) cross sections. **A:** bSEM images showing how the enamel was divided into mesial and lateral regions by drawing a line from the mesial cervical margin to the lateral cervical margin and drawing a line perpendicular from its midpoint. The mesial, lateral, and total cross-sectional areas (mm^2) were determined by outlining the enamel on Photoshop (Fam83h$^{+/+}$ n=8; Fam83h$^{Tr/Tr}$ n=10; see Fig. S24). **B:** Table showing the average areas and ρ values (T test). All ρ values 0.01 or below were considered to be significant (*). **C:** Plot of the average lateral, mesial, and total surface areas of Fam83h$^{+/+}$ (n=8) and Fam83h$^{Tr/Tr}$ (n=10) mice. Significant differences were observed between the wild-type and the Fam83h homozygous truncation (Fam83h$^{Tr/Tr}$) incisors in their lateral and total cross-sectional areas, but not in the mesial enamel.

Fig. 9. Micro and Nano Hardness Plots. Indents in dentin, inner enamel, middle enamel, and outer enamel on 7-week mandibular incisor cross sections at the level of the alveolar crest (level 8). **A:** Plot of the average calculated Knoop Hardness Value for Fam83h$^{+/+}$, Fam83h$^{+/Tr}$ and

Fam83h$^{Tr/Tr}$ mice for dentin and enamel. Knoop hardness=14.229p/d^2; p=force (kgf) applied; d=length (mm) of the long diagonal of the indent. **B:** Average calculated Knoop hardness values with standard deviations (Micro-hardness values of individual indents see Fig. S25). **C:** SEM images of selected micro-indented samples to show indent locations. Images of the entire set of samples are provided in Fig. S25. **D:** Plot of the average calculated nanohardness values in gigapascals: Gpa = 14.229p/d^2; p=force (N) applied; d=length (mm) of the long diagonal of the indent (Fig. S26). A $\rho<0.01$ was considered significant. All ρ values were above 0.01 and did not support a hypothesis of significant hardness differences among the three genotypes. **E:** Average nanohardness values with standard deviations. **F:** SEM images of selected nano-indented samples to show indent locations (indicated by diamond shapes). Images of the entire set of samples are provided in Fig. S27.

Fig. 10. Histology of Mandibular Incisor Longitudinal Sections at 7-weeks. **Top:** Apical region showing the secretory stage starting at the onset of mineralization. **Bottom:** Central region showing the end of the secretory stage, the transition stage (delineated by arrowheads), and early maturation stage. Ameloblast histology appears similar in the Fam83h$^{+/+}$, Fam83h$^{+/Tr}$, and Fam83h$^{+/Tr}$ mice, although the ameloblasts give the impression of being shorter in the Fam83h$^{+/Tr}$ and Fam83h$^{Tr/Tr}$ mice.

Fig. 11. Histology of Secretory Stage Ameloblasts on the Lateral Aspect of 7-weeks Mandibular Mouse Incisors. **A:** Cross-sections of 3 wild-type incisors at Level 2. Arrowheads indicate Tomes' Processes extending into enamel. **Key:** Am, ameloblasts; d, dentin; e, enamel; od, odontoblasts; p, pulp. Ameloblasts (Am) covering the lateral aspect of wild-type mandibular incisors show prominent Tomes' processes (arrowheads). **B:** Comparable images from four

Fam83h$^{Tr/Tr}$ incisors showing ameloblast lateral membranes apparently lacking Tomes Processes (circled).

APPENDICES

Additional Supporting Information may be found online in the supporting information tab for this article:

Supplemental Data File 1:

Figure S1. Generating and Genotyping the Fam83h$^{Tr/Tr}$ Mouse.
Figure S2. Wild-Type Mouse Fam83h Gene Sequence and Structure.
Figure S3. Knockin intermediate following removal of selection genes by Flp-FRT recombination.
Figure S4. Final Fam83h^{TR} Knockin Sequence.
Figure S5. bSEMs of mandibular molars at 7-weeks.
Figure S6. Histology of Fam83h$^{+/+}$ (WT), Fam83h$^{Tr/Tr}$, and Fam83h$^{Tr/-}$ Molars at Days 5, 11, and 14.
Figure S7. SDS-PAGE of enamel proteins at D5, D11, and D14.

Supplemental Data File 2:

Figure S8. Backscattered SEM images of mandibular incisor cross-sections taken at ~1 mm increments (WT-953; Het-986; Null-X) starting at the apical end of the incisor (low magnification).
Figure S9. Backscattered SEM images of mandibular incisor cross-sections taken at ~1 mm increments (WT-953; Het-986; Null-X) starting at the apical end of the incisor (middle magnification).
Figure S10. Histology of Fam83h$^{+/+}$ Maxillary Incisor at 7-weeks (WT17).
Figure S11. Backscattered SEM images of mandibular incisor cross-sections of Het-950 taken at ~1 mm increments starting at the apical end of the incisor.
Figure S12. Backscattered SEM images of mandibular incisor cross-sections of Het-951 taken at ~1 mm increments starting at the apical end of the incisor.
Figure S13. Backscattered SEM images of mandibular incisor cross-sections of Het-952 taken at ~1 mm increments starting at the apical end of the incisor.
Figure S14. Backscattered SEM images of mandibular incisor cross-sections of Het-976 taken at ~1 mm increments starting at the apical end of the incisor.
Figure S15. Backscattered SEM images of mandibular incisor cross-sections of Het-982 taken at ~1 mm increments starting at the apical end of the incisor.
Figure S16. Backscattered SEM images of mandibular incisor cross-sections of Het-986 taken at ~1 mm increments starting at the apical end of the incisor.
Figure S17. Backscattered SEM images of mandibular incisor cross-sections of Null-932 taken at ~1 mm increments starting at the apical end of the incisor.
Figure S18. Backscattered SEM images of mandibular incisor cross-sections of Null-956 taken at ~1 mm increments starting at the apical end of the incisor.

Figure S19. Backscattered SEM images of mandibular incisor cross-sections of Null-957 taken at ~1 mm increments starting at the apical end of the incisor.
Figure S20. Backscattered SEM images of mandibular incisor cross-sections of Null-974 taken at ~1 mm increments starting at the apical end of the incisor.
Figure S21. Backscattered SEM images of mandibular incisor cross-sections of Null-995 taken at ~1 mm increments starting at the apical end of the incisor.
Figure S22. Backscattered SEM images of mandibular incisor cross-sections of Null-X taken at ~1 mm increments starting at the apical end of the incisor.
Figure S23. Backscattered SEM images of mandibular incisor cross-sections of Wild-Type-953 taken at ~1 mm increments starting at the apical end of the incisor.
Figure S24. Enamel area on 7-week mandibular incisor level 8 (alveolar crest) cross sections.
Figure S25. Microhardness Testing. bSEM images of surfaces tested & Microhardness Table.
Figure S26. Nanohardness Test Table
Figure S27. Nanohardness Testing. SEM images of level 8 cross-sections of 7-week mandibular incisors in Fam83h$^{+/+}$ (n=6), Fam83h$^{+/Tr}$ (n=6) and Fam83h$^{Tr/Tr}$ (n=5) for nanohardness testing.

Supplemental Data File 3:
Figure S28. Histology of Fam83h$^{Tr/Tr}$ Maxillary Incisor at 7-weeks (F11).
Figure S29. Histology of Fam83h$^{Tr/+}$ Maxillary Incisor at 7-weeks (F04).
Figure S30. Histology of Fam83h$^{+/+}$ Maxillary Incisor at 7-weeks (WT17).
Figure S31. Histology of Fam83h$^{Tr/Tr}$ Mandibular Incisor at 7-weeks (F08B1).
Figure S32. Histology of Fam83h$^{Tr/Tr}$ Mandibular Incisor at 7-weeks (F08B2).
Figure S33. Histology of Fam83h$^{Tr/Tr}$ Mandibular Incisor at 7-weeks (F09B1).
Figure S34. Histology of Fam83h$^{Tr/Tr}$ Mandibular Incisor at 7-weeks (F09B2).
Figure S35. Histology of Fam83h$^{Tr/Tr}$ Mandibular Incisor at 7-weeks (F10B1).
Figure S36. Histology of Fam83h$^{Tr/Tr}$ Mandibular Incisor at 7-weeks (F10B2).
Figure S37. Histology of Fam83h$^{Tr/Tr}$ Mandibular Incisor at 7-weeks (F06B1).
Figure S38. Histology of Fam83h$^{Tr/Tr}$ Mandibular Incisor at 7-weeks (F06B2).
Figure S39. Histology of Fam83h$^{Tr/Tr}$ Mandibular Incisor at 7-weeks (F07B1).
Figure S40. Histology of Fam83h$^{Tr/Tr}$ Mandibular Incisor at 7-weeks (F07B2).
Figure S41. Histology of Fam83h$^{Tr/+}$ Mandibular Incisor at 7-weeks (F03B1).
Figure S42. Histology of Fam83h$^{Tr/+}$ Mandibular Incisor at 7-weeks (F03B2).
Figure S43. Histology of Fam83h$^{Tr/+}$ Mandibular Incisor at 7-weeks (F04B1).
Figure S44. Histology of Fam83h$^{Tr/+}$ Mandibular Incisor at 7-weeks (F04B2).
Figure S45. Histology of Fam83h$^{+/+}$ Mandibular Incisor at 7-weeks (WT17B1).
Figure S46. Histology of Fam83h$^{+/+}$ Mandibular Incisor at 7-weeks (WT17B2).
Figure S47. Histology of Fam83h$^{+/+}$ Mandibular Incisor at 7-weeks (WT18B1).
Figure S48. Histology of Fam83h$^{+/+}$ Mandibular Incisor at 7-weeks (WT18B2).

Supplemental Data File 4:
Figure S49. Histology of Fam83h$^{Tr/Tr}$ and Fam83h$^{+/+}$ Mandibular Incisor at 7-weeks (low magnification).
Figure S50. Histology of Fam83h$^{+/+}$ Mandibular Incisor at 7-weeks (WT4).
Figure S51. Histology of Fam83h$^{+/+}$ Mandibular Incisor at 7-weeks (WT5).
Figure S52. Histology of Fam83h$^{+/+}$ Mandibular Incisor at 7-weeks (WT6).

Figure S53. Histology of Fam83h$^{Tr/Tr}$ Mandibular Incisor at 7-weeks (F8).
Figure S54. Histology of Fam83h$^{Tr/Tr}$ Mandibular Incisor at 7-weeks (F9).
Figure S55. Histology of Fam83h$^{Tr/Tr}$ Mandibular Incisor at 7-weeks (F10).
Figure S56. Histology of Fam83h$^{Tr/Tr}$ Mandibular Incisor at 7-weeks (F11).
Figure S57. Histology of 7-week Fam83h$^{+/+}$ Mandibular Incisor Cross Sections (WT4).
Figure S58. Histology of 7-week Fam83h$^{Tr/Tr}$ Mandibular Incisor Cross Sections (F8).
Figure S59. Histology of 7-week Fam83h$^{Tr/Tr}$ Mandibular Incisor Cross Sections (F9).
Figure S60. Histology of 7-week Fam83h$^{Tr/Tr}$ Mandibular Incisor Cross Sections (F10).
Figure S61. Histology of 7-week Fam83h$^{Tr/Tr}$ Mandibular Incisor Cross Sections (F11).

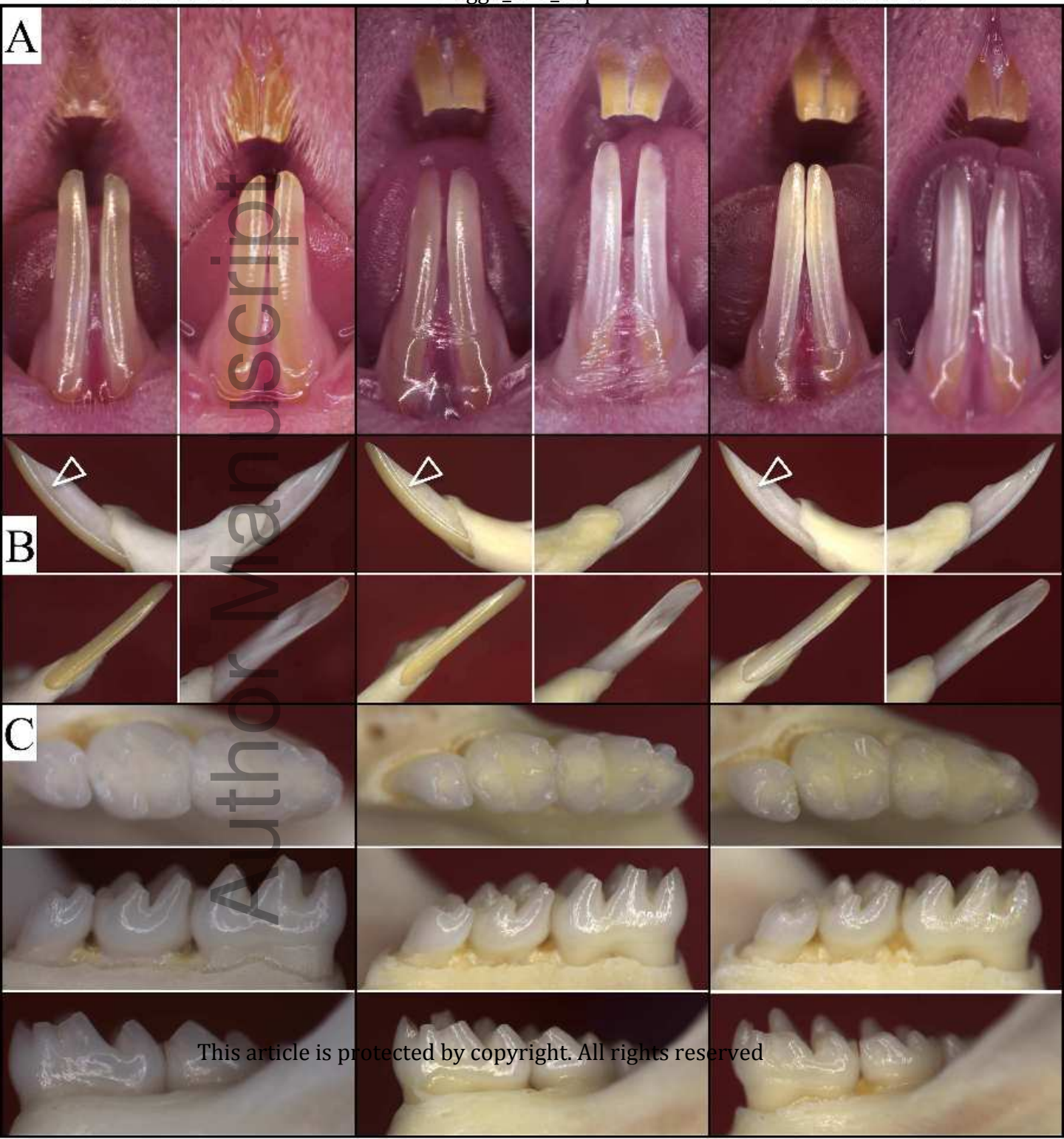

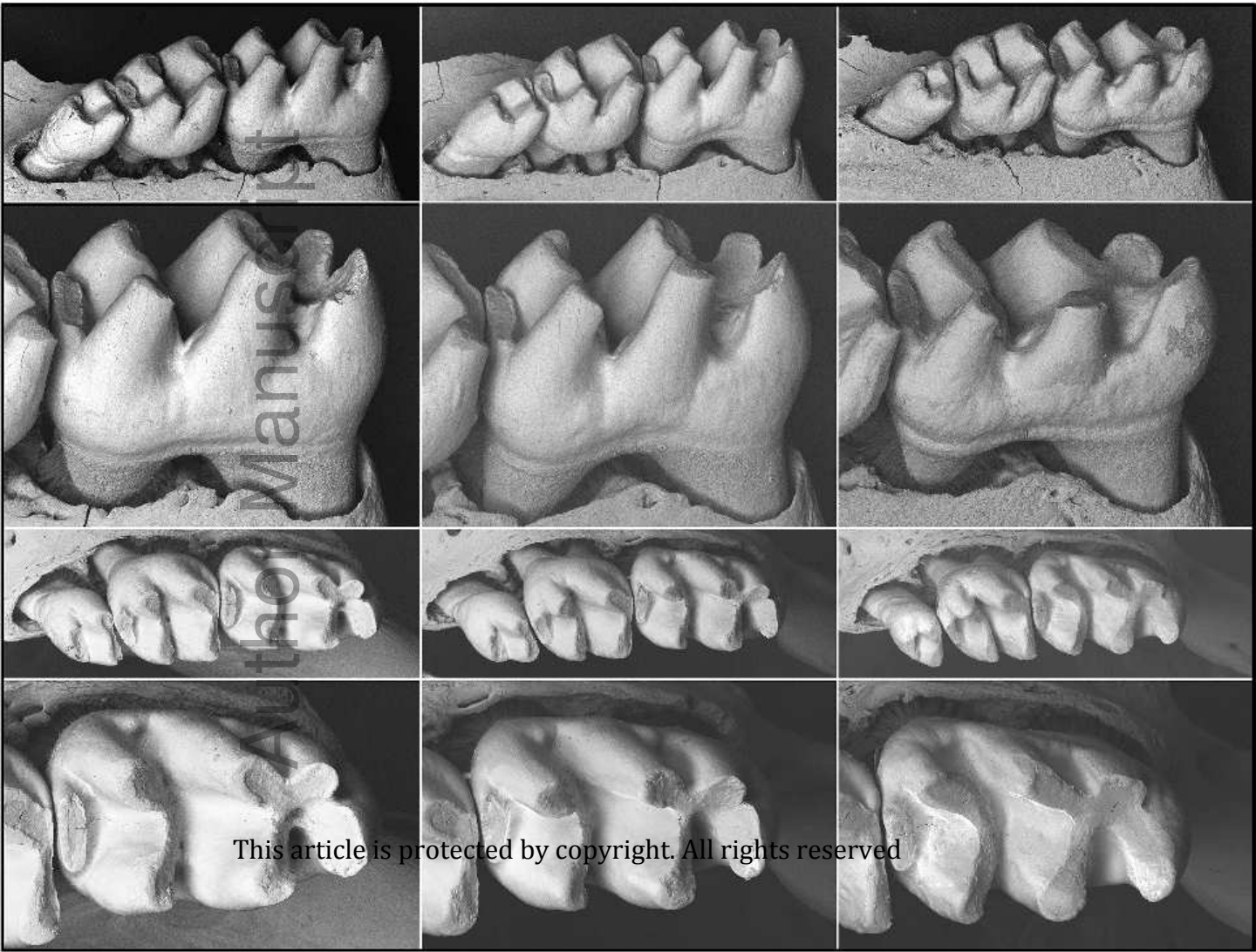

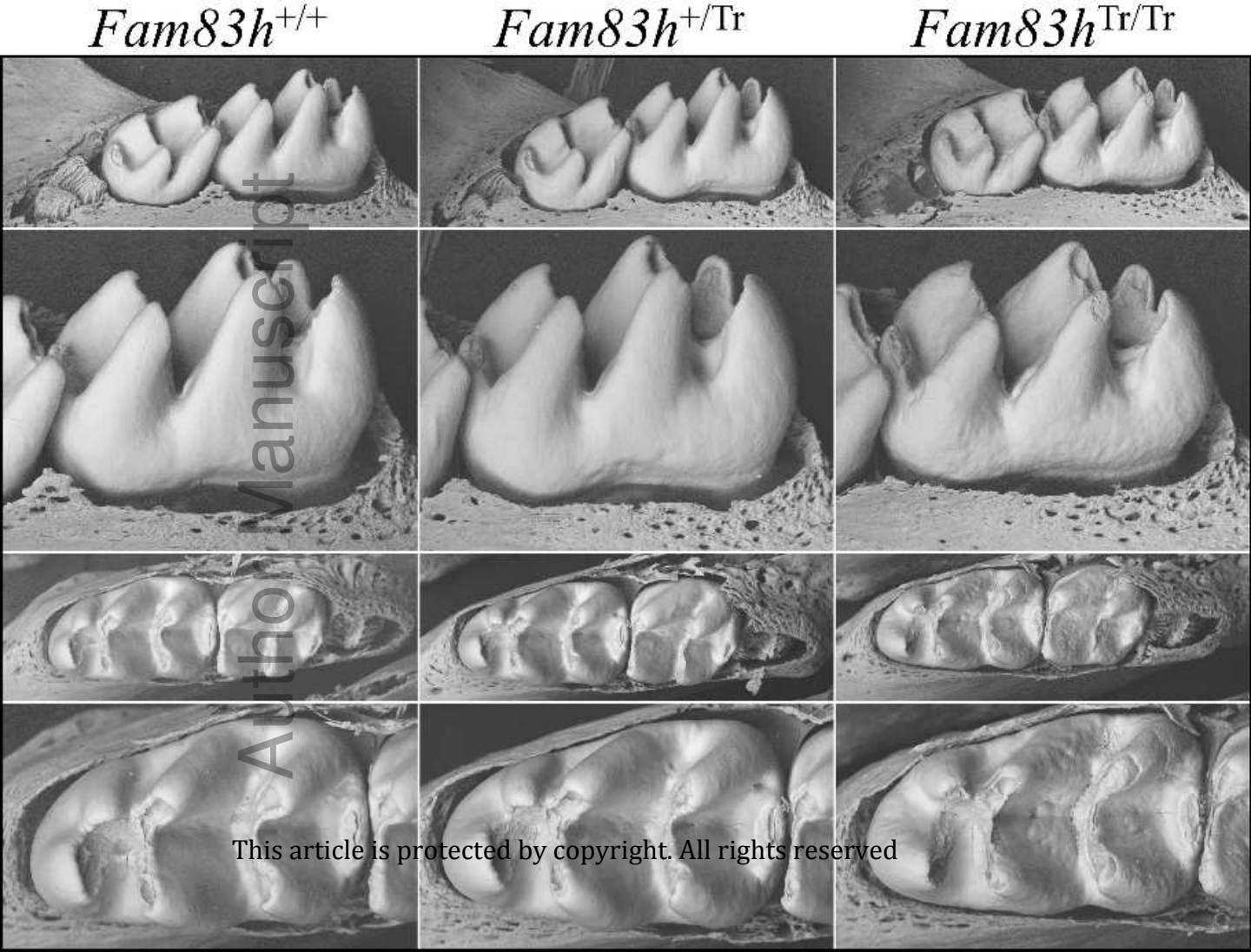

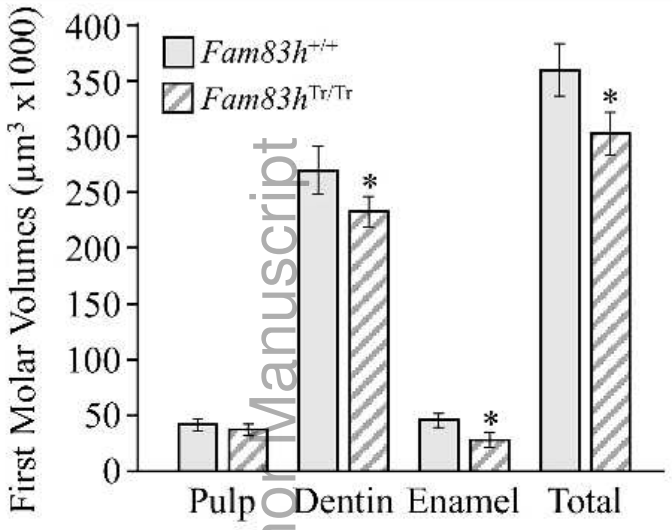

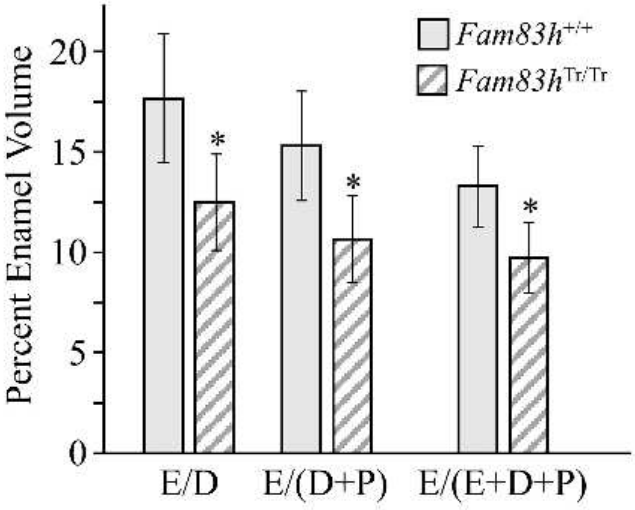

First Molar Volumes (μm³)

	Fam83h$^{+/+}$	*Fam83h*$^{Tr/Tr}$	*p*
Pulp	42608± 4946	39713± 4818	0.32864
Dentin	271177±21482	235539±13738	0.00691*
Enamel	47619± 6355	29525± 6179	0.00054*
Total	361404±23642	304777±19600	0.00111*

% Enamel Volume

	Fam83h$^{-/-}$	*Fam83h*$^{Tr/Tr}$	*p*
E/D	17.7±0.032	12.5±0.024	0.01077*
E/(D+P)	15.3±0.027	10.7±0.022	0.00960*
E/(E+D+P)	13.2±0.020	9.7±0.018	0.00889*

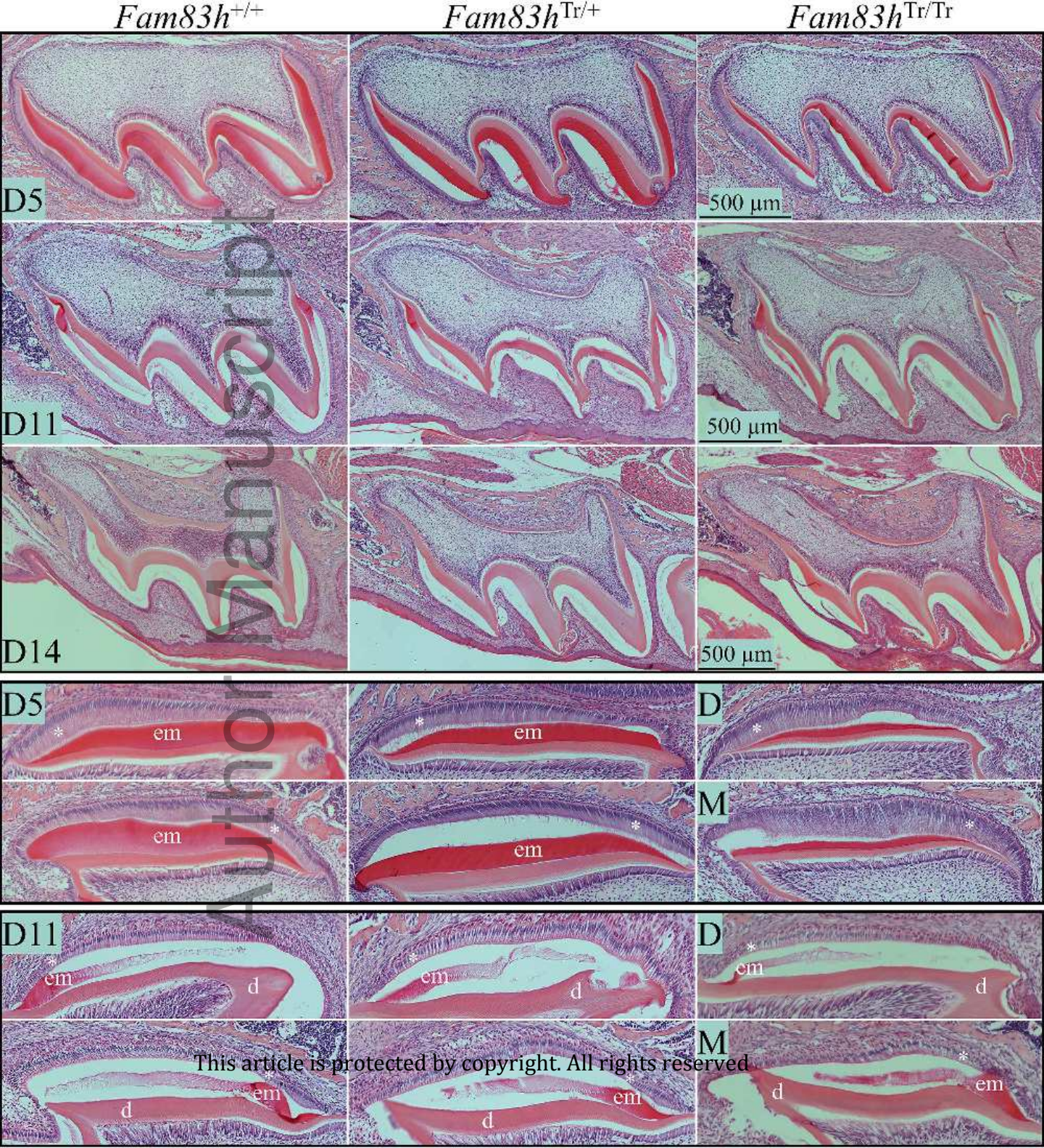

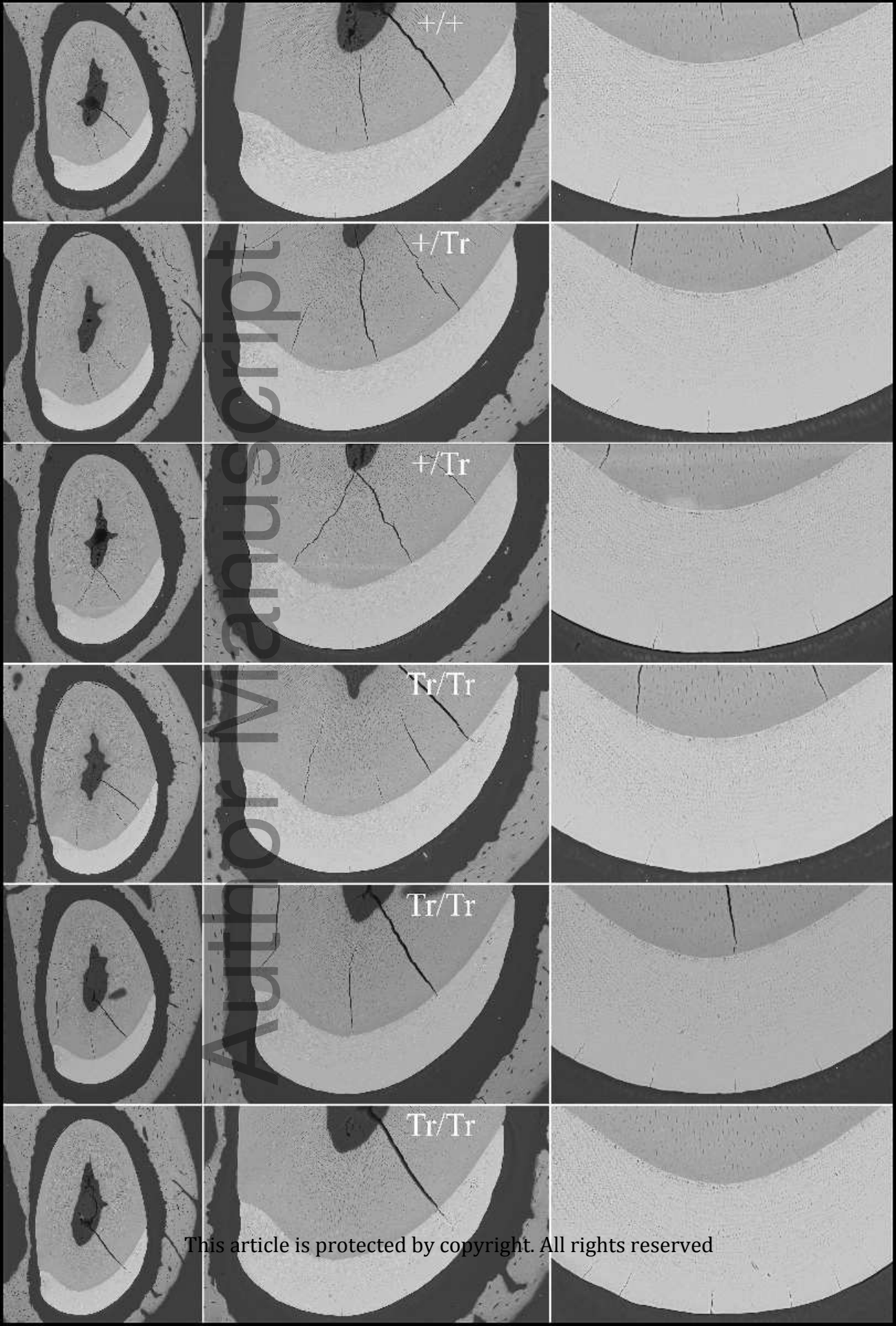

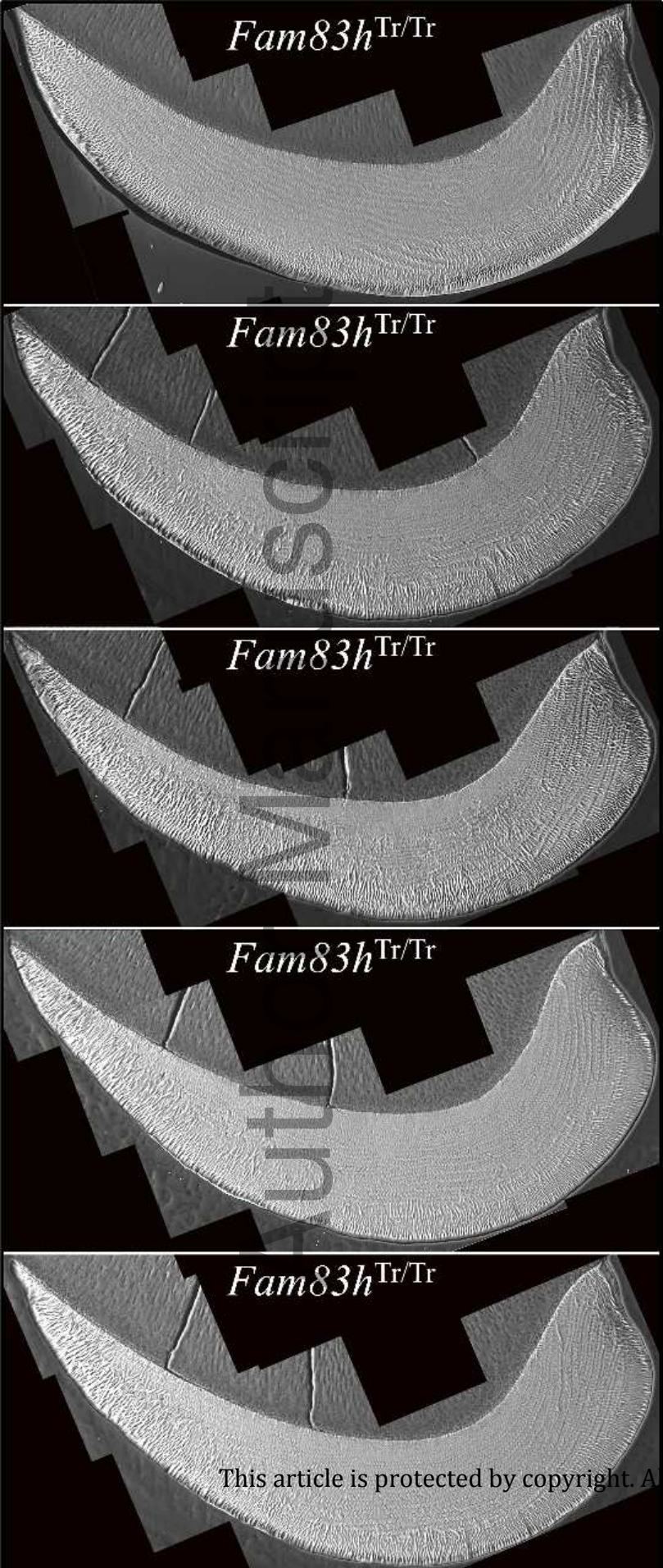

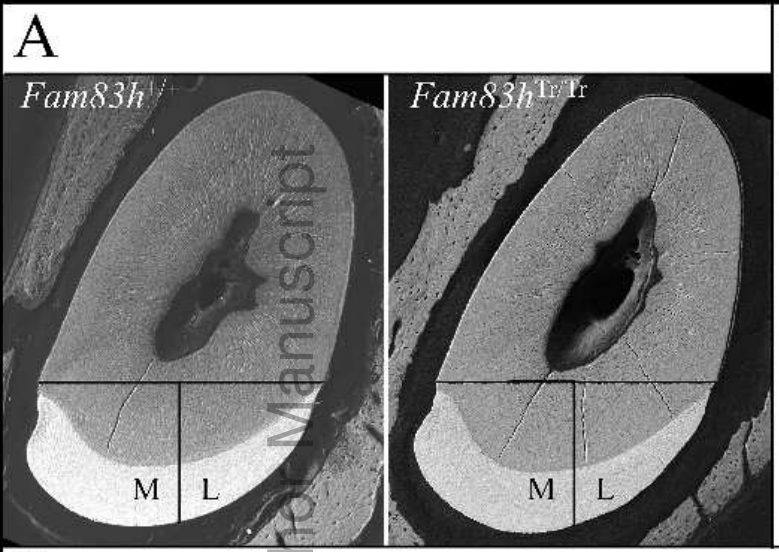

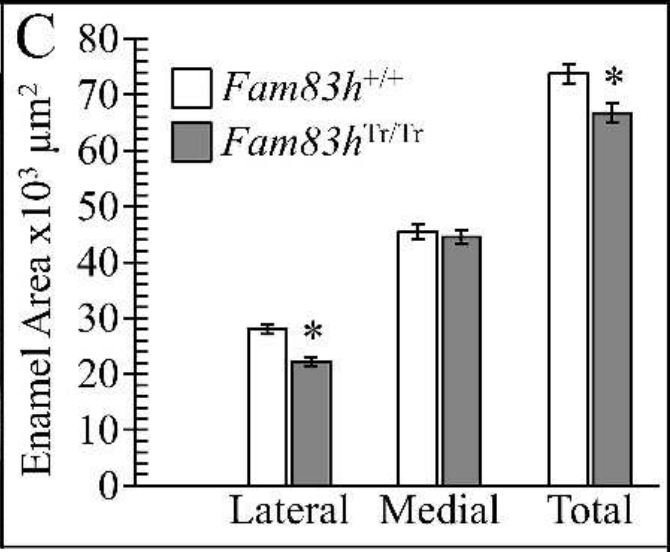

B

	Fam83h$^{+/+}$	*Fam83h*$^{Tr/Tr}$	T test
Lateral	28124.8±1737.1	22262.4±1512.4	9.8×10^{-7} *
Medial	45578.4±2493.7	44509.6±2126.4	3.4×10^{-1}
Total	73703.2±3519.1	66772.0±3450.3	6.8×10^{-4} *

A

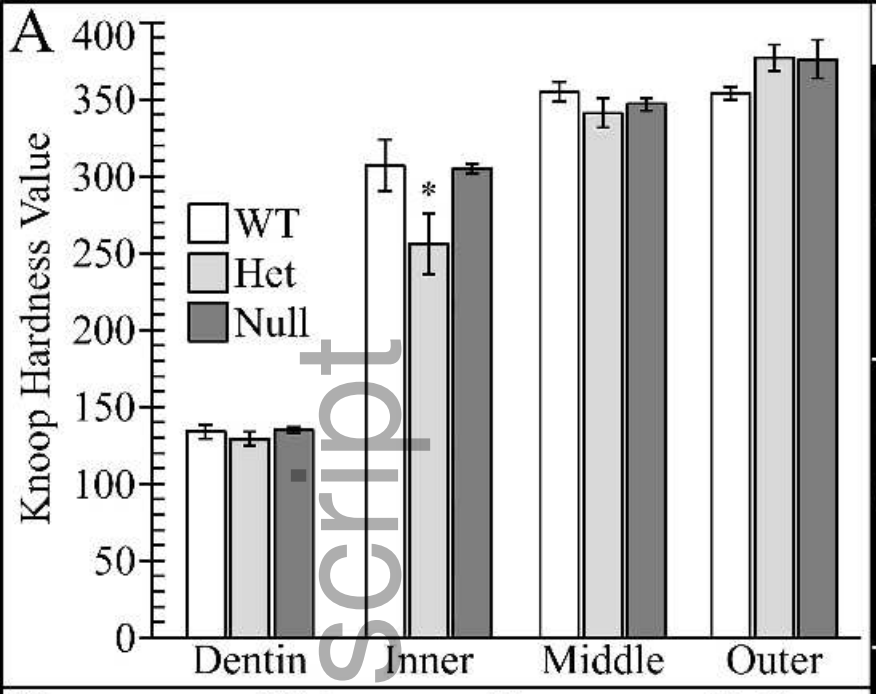

B

	WT	Het	Null
Dentin	134.4± 8.6	128.7± 8.6	135.5±4.3
Inner	307.4±34.2	255.9±39.5	304.8±6.2
Middle	354.6±13.1	340.8±18.5	346.7±7.9
Outer	353.7± 8.3	377.2±16.5	376.4±24.7

C

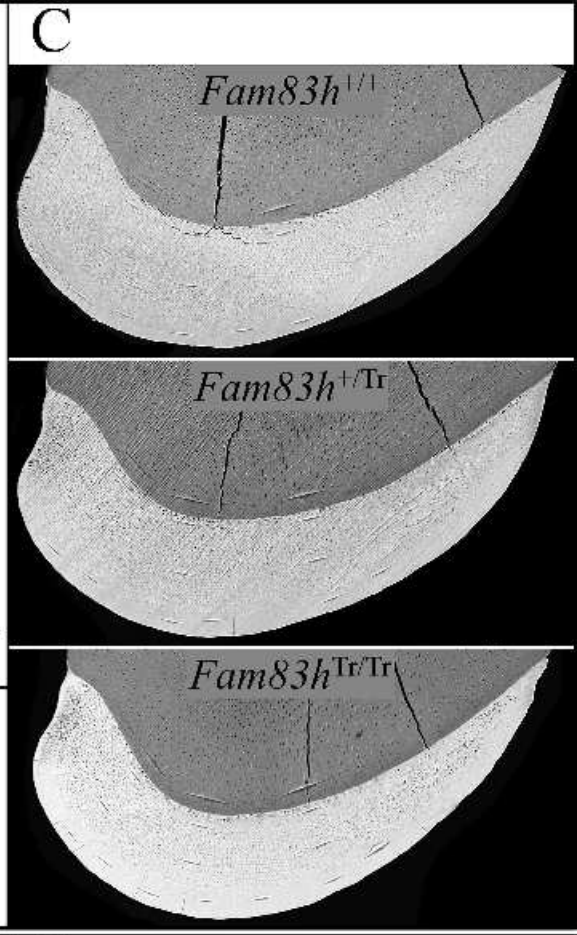

D

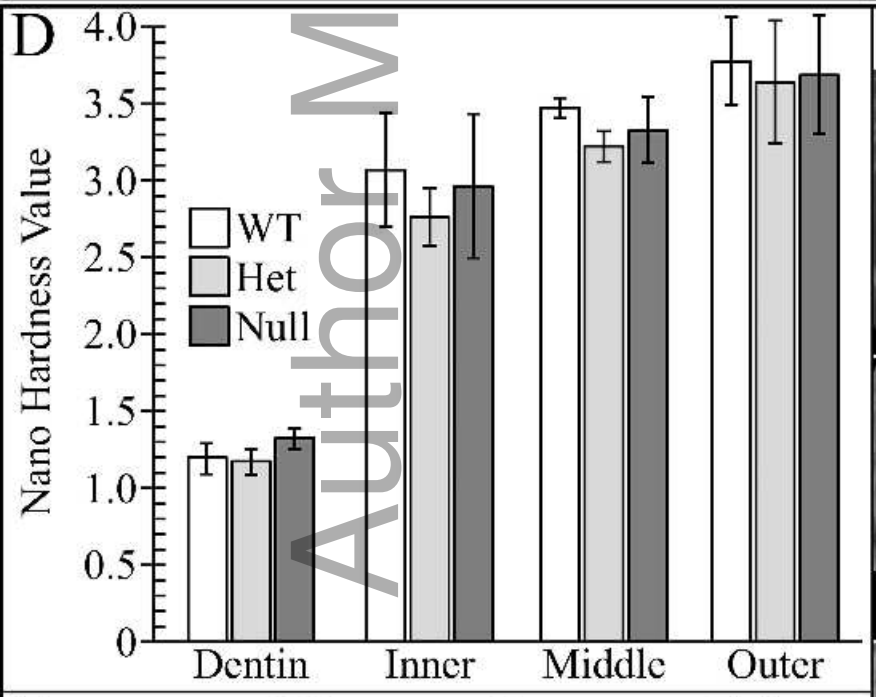

E

	WT	Het	Null
Dentin	1.20±0.10	1.18±0.08	1.32±0.07
Inner	3.08±0.37	2.76±0.19	2.96±0.47
Middle	3.47±0.06	3.22±0.10	3.32±0.21
Outer	3.78±0.29	3.63±0.40	3.69±0.39

F